Technische Universität München

Fakultät für Physik

Master Thesis

Design and Characterization of an UV-Lasersystem for Rydberg Experiments with Potassium

Anne-Sophie Walter

Thesis conducted at the Max-Planck Institute for Quantum Optics

First evaluator	Prof. Dr. R. Gross
Second evaluator	Prof. Dr. I. Bloch
Supervisor	Dr. C. Gross
Thesis submitted on	November 22, 2018

Contents

Abstract

In this work we present the design, construction and initial characterization of a setup for a one-photon transition to Rydberg states in Potassium. The work describes the design of two doubling cavities which allow the conversion of infrared to UV light, tunable between 285.5 and 288.5 nm. We characterize the frequency-stabilized linewidth of the infrared laser to be 160 kHz and achieve output powers of at least 8 W after a Raman Fiber Amplifier. The performance of the constructed first doubling cavity yields output powers of up to 4 W which exactly fits with the calculations.

Introduction

The first experimental realization of a Bose-Einstein condensate [1], [2], [3] and the achievement of cooling to Fermi degeneracy [4],[5], [6] have set the basis for significant growth of the research field around ultracold atoms. These systems of atoms present a clean and controllable platform. They are used for the exploration of phenomena such as the existence of coherent matter waves or for the simulation of complex many-body systems. Historically, two developments broadened the possible range of physics accessible with these systems: the use of Feshbach resonances, and optical traps. Feshbach resonances allow to tune the interaction strength between the atoms and with optical traps, they can be confined in particular configurations such as lattices. Benchmark experiments following these new methods are the measurement of the superfluid to Mott-insulator transition [7], investigations on the BEC-BCS crossover [8] and the Ising model [9].

Quantum gas microscopes are another invaluable tool in the research field around ultracold atoms. They enable single-site detection and were first implemented for bosons [10], [11] and later for fermions [12], [13], [14], [15], [16]. This new imaging tool allows to locate individual atoms but also provided a basis for methods to manipulate these atoms with the help of strongly focused beams or spatial modulators [17], [18], [19]. The manipulation and visualization tools provided by ultracold atoms allow to engineer a range of easily accessible and controllable quantum systems which can provide insight into the behavior of more complex quantum systems. This methodology is called quantum simulation and enables the study of strongly correlated systems which were until then only accessible in condensed matter or nuclear physics.

However, using Feshbach resonances limits the simulated quantum systems to those with short-range interactions. Possibilities to widen the range and nature of interactions, are the use of atoms with permanent magnetic dipoles [20], [21], [22], [23], dipolar molecules [24], or Rydberg atoms [25]. In these Rydberg atoms one or more electrons are excited to a high-lying energy level which induces long-range interactions. These interactions cause the so called Rydberg blockade: two Rydberg atoms cannot be simultaneously excited within a certain distance of one another. Instead of a pure Rydberg state, it is also possible to only add a small admixture of Rydberg state to the ground state of a neutral atom. This is called Rydberg dressing. Both Rydberg atoms and Rydberg dressed atoms can be achieved by optical coupling to laser light. There are two possible methods to implement this coupling. The first is to directly go from the ground state to the Rydberg state using one laser and the so-called a one-photon transition. The second possibility is to introduce an intermediate state which requires two lasers, one for the coupling to the intermediate state and the other for the coupling to the Rydberg state, this methodology is therefore called a two-photon transition.

The laboratory in which this thesis was conducted aims at implementing both methods for the excitation of Potassium atoms. In this context, the aim of this thesis is the design and characterization of the setup necessary for the one-photon transition. Work on the setup for the two-photon transition in Potassium atoms is described in [26].

First, we give a quick introduction on Rydberg atoms, some of their characteristics and interactions, and move on to Rydberg dressing. As it is necessary to rely on frequency doubling to obtain the necessary high power light fields with short wavelengths, theory of second harmonic generation is described in the second Chapter: we discuss non-linear effects in media, the necessary phase matching condition and finally the harmonic conversion of Gaussian beams. In the experiment, it is important to have high powers of UV light as the interaction strength increases with the light intensity. Therefore, cavities have to be built around the non-linear medium which generates second harmonic light, they are the focus of Chapter 3. Chapter 4 describes the stability

and self-consistency of cavities in ray optics, moves on to a more accurate description through Gaussian beams, then looks into detail at the cavities important to this thesis, to conclude with the fundamental quantities which characterize them. For the frequency and length stabilization of these cavities and the laser, the locking methods of interest are presented in Chapter 5.

For the construction of the two doubling cavities, from infrared to green, and then to UV light, we conduct a parameter optimization in Chapter 6 to allow for a stable geometry and impedance matching. Chapter 7 describes the experimental setup and starts off with the infrared laser source, its frequency stabilization and linewidth characterization and the amplification stage by way of a Raman Fiber Amplifier (RFA). Finally, the first doubling stage, from infrared to green light is described in Chapter 8, and the performance is compared to the calculations from Chapter 6.

1 Rydberg Atoms

Rydberg atoms are atoms with one or more electrons excited to a high-lying energy level. This excitation can be induced by various means such as radiative recombination of electrons with ions, collisions of electrons with ground state atoms or by optical coupling to laser light [27]. The spatial separation between electron and atomic core leads to the exaggerated properties of Rydberg atoms. For instance, this separation implies that there is only a small overlap between the electron's and core's wavefunctions leading to lifetimes of the excited state of a few milliseconds which enable long coherence times in experiments. In the following, we restrict ourselves to alkali atoms which have their outermost electron in an s-orbital and to Rydberg excitation through optical coupling to laser light. We first describe the energy scheme of such atoms, the lifetime of the Rydberg states and follow with the interaction between two atoms in such a high-lying state. Finally, moving away from resonantly excited Rydberg states, we discuss Rydberg dressed states and demonstrate their reduced interaction strength and increased lifetime.

1.1 Level Scheme and Lifetime

Rydberg atoms with one electron populating a high-lying energy level are similar to the hydrogen atom. However, the point charge of the proton in hydrogen needs to be replaced by a finite-sized ionic core. The outer electron in the Rydberg atom lies outside the ionic core. Indeed, the mean square radius of Rydberg atoms scales as $\langle r^2 \rangle^{1/2} \propto n^2$. For large n, this puts the electron far outside the core. Therefore we can use quantum defect theory to calculate the correction to the hydrogen model [28]. The resulting binding energies of the valence electron with quantum numbers n, L, J are:

$$E_{n,L,J} = E_{ion} - \frac{R_*}{\left(n - \delta_{n,L,J}\right)^2} \equiv E_{ion} - \frac{R_*}{(n^*)^2}, \tag{1.1}$$

where E_{ion} is the ionization threshold and R_* the effective Rydberg constant corrected by the reduced mass $R_* = \frac{1}{1+\frac{m_e}{m}} \cdot R_{\text{inf}}$ with m as the atom's nuclear mass, m_e the electron's mass and R_{inf} the Rydberg constant. The effective principal quantum number n^* takes into account the quantum defect correction $\delta_{n,L,J}$ induced by the screening of the electrons around the core. This correction is determined by fitting empirical models to experimental data of the energy spectrum. It is highest for s-states as the wavefunction is closest to the core and decreases with higher angular qunatum number L, generally becoming negligible for $L > 4$ [29]. The resulting level scheme of the outer valence electron for Potassium 39 is shown in Fig. 1.1.

For optical coupling to a Rydberg state, there are two possibilities either by a two or one-photon transition. The first introduces an intermediate level before coupling to the Rydberg state and requires two lasers. The second possibility, the one-photon transition couples directly to the Rydberg state. In the laboratory both possibilities will be realized although this work focuses on the latter. For a discussion of the two-photon transiton in Potassium 39 we refer to [26]. This direct transition corresponds to wavelengths in the UV. To obtain high power UV light, it is best to start with an infrared laser source and go through two doubling cavities. Transitions for the different possibilities for Rydberg excitation are shown in Fig. 1.1.

Once an electron is excited to a Rydberg state, this state will have a finite lifetime and decay back to the ground state or to another Rydberg state. The value of this lifetime is important as it sets a limit to the timescales on which an experiment can be conducted coherently. The decay to the ground states $1/\tau_{rad}$ is accompanied by the emission of an UV photon. The decay

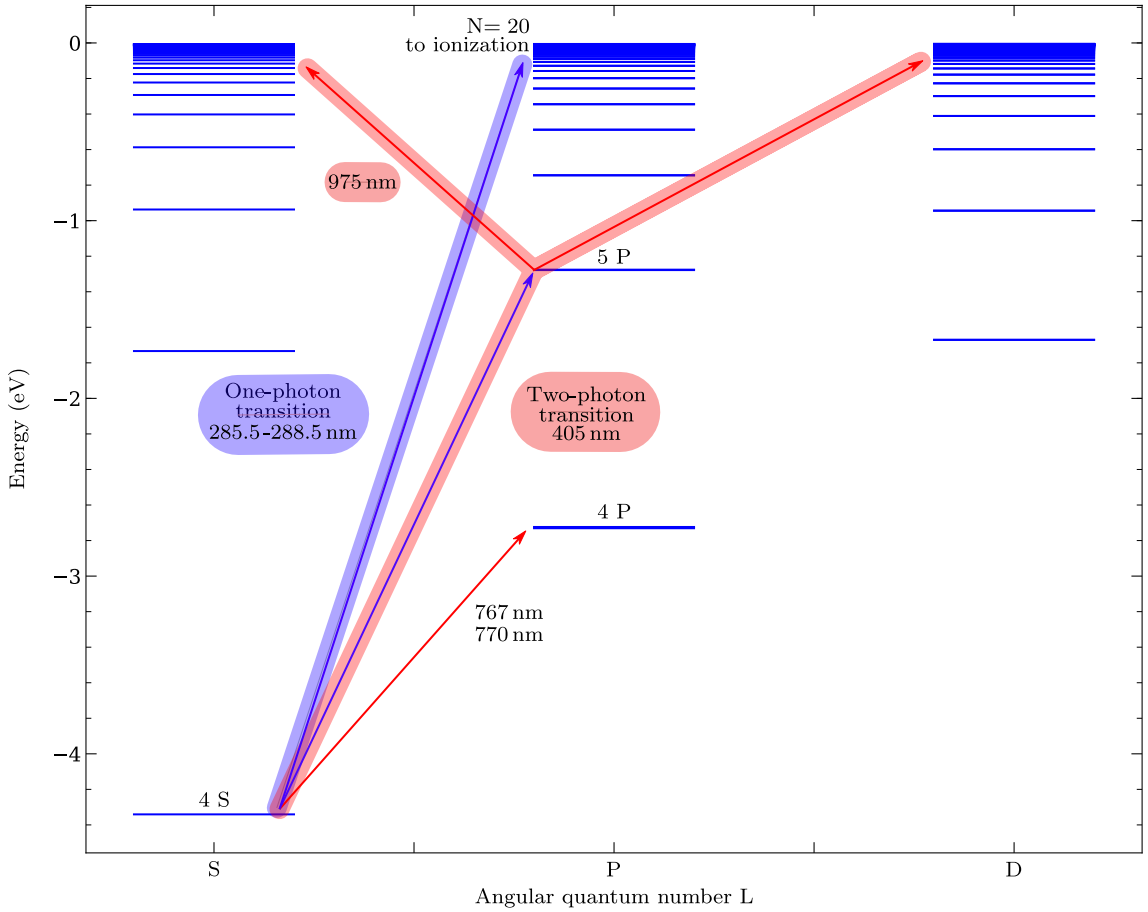

Figure 1.1: Energy levels of ^{39}K: Displayed are the one and two-photon transitions to Rydberg states and the transition used for cooling of the MOT, imaging etc. [30], [31]

to neighboring Rydberg states via stimulated emission of a microwave photon to the black-body radiation background yields a rate $1/\tau_{BB}$ [27]. The overall lifetime τ is then composed of both contributions:

$$\tau = \left(\frac{1}{\tau_{rad}} + \frac{1}{\tau_{BB}} \right)^{-1}. \tag{1.2}$$

The radiative lifetime τ_{rad} scales as n^{*3} for alkali atoms and can be of the order of milliseconds for high $n \sim 100$. This high value can be understood from the decreasing overlap of the ionic core's and electron's wavefunctions with increasing quantum number n. Compared to the radiative lifetime, the blackbody lifetime is the restrictive factor as it scales with n^{*2}. Indeed with higher n^* the Rydberg atom becomes more sensitive to external fields. The lifetime in an environment with blackbody radiation at temperature T is given by [27]:

$$\tau_{BB}(n,T) = \frac{3\hbar n^{*2}}{4\alpha^3 k_B T}, \tag{1.3}$$

with α the fine structure constant and k_B the Boltzmann constant.

1.2 Interaction between two Rydberg States

In order to obtain long-range interactions in a system, different possibilities exist. One approach is to start with weakly interacting particles and switch on the interactions by tuning Feshbach resonances [32] or using high-finesse resonators [33]. Another way is to use particles like polar molecules or ions which are already strongly interacting. However, the strong interactions between the ions fix the particles in certain configurations, while molecules are difficult to cool to low temperatures. As we will see below, Rydberg-Rydberg interactions present a solution to this as their interaction strength is comparable to ionic systems while being switchable [25].

The interactions between atoms are strongly modified when they are excited to high-lying Rydberg states. In Rydberg atoms the large spatial separation between valence electron and ionic core leads to a high polarizability scaling with n^{*7}. Due to this high polarizability, Rydberg atoms are very sensitive to external electric fields, including the multipole moments of neighboring Rydberg atoms. The interaction potential between two Rydberg atoms separated by a distance R can be expanded in a Laurent series. Being neutral atoms, the first two terms involving the charge vanish. The first non-vanishing term is the dipole-dipole interaction:

$$V(\mathbf{r}_1, \mathbf{r}_2) = \left(1 - 3\cos^2\theta_{ij}\right) \frac{d_i d_j}{4\pi\varepsilon_0 R^3}, \tag{1.4}$$

with d_i and d_j being the electric dipole operators and θ_{ij} the angle between the interatomic axis and the quantization axis of the atoms. This is the potential for the interaction between Rydberg atoms in different Rydberg states. If, however, the two atoms are in the same Rydberg state, with an optical detuning much larger than the interaction strength, it is possible to solve the system in perturbation theory leading to a van-der-Waals interaction of the form [34]:

$$V_{vdW}(R) = -\frac{C_6}{R^6}, \tag{1.5}$$

where the coefficient C_6 scales as n^{*11}. For Rydberg states with typical $n^* \sim 40$ this scaling is very favorable and the coefficient C_6 grows large. The atoms are optically coupled to the high-lying Rydberg state through coupling to laser light. We consider the case for which the interaction between the two Rydberg atoms is larger than the decay rate Γ of the Rydberg state and the Rabi frequency Ω with which the transition is driven:

$$V_{vdW}(R) = -\frac{C_6}{R^6} > \hbar \cdot max\{\Gamma, \Omega\}. \tag{1.6}$$

If this applies, the interaction causes the pairstate of double excitation to significantly shift in energy and causes the laser to become off-resonant to the transition. Therefore, it is not possible to excite a second Rydberg atom within a certain distance of a first. This phenomenon is called Rydberg blockade. In some experiments, the Rabi frequency is larger than the decay rate of the Rydberg atom, making Ω the determining value for the so called blockade radius:

$$R_b = \left(\frac{C_6}{\hbar\Omega}\right)^{1/6}. \tag{1.7}$$

Its values are of the order of a few micrometers. A schematic drawing of the energy shift out of resonance in the pair state picture is shown in Fig. 1.2a.

1.3 Rydberg Dressing

With these Rydberg atoms, it is hard to probe dynamical systems because of the limiting lifetimes. To achieve longer lifetimes which allow measurements in the dynamical regime, it is possible to couple the ground state $|g\rangle$ to the Rydberg state $|r\rangle$ off-resonantly, leading to a ground

state with a small Rydberg state admixture [35]:

$$|\psi\rangle = \alpha\,|g\rangle + \beta\,|r\rangle\,, \tag{1.8}$$

where $\beta = \Omega/2\Delta$, with Δ the detuning and Ω the Rabi frequency. Rydberg dressing occurs in the regime where $\beta \ll 1$. The resulting interaction potential between two Rydberg dressed atoms can be obtained by treating the light field as a small perturbation and is of the form:

$$U(R) = \frac{U_0}{1 + \left(\frac{R}{R_c}\right)^6}, \tag{1.9}$$

where $U_0 = 2\hbar\Delta\beta^4 = \hbar\Omega^4/8\Delta^3$ is the saturation value of this soft-core potential for $R \to 0$. The cut-off radius $R_c = |C_6|/2\hbar|\Delta|^{1/6}$ sets the scale at which the value of the dressed potential changes (see Fig. 1.2b). This equation is valid for a repulsive van-der-Waals interaction $C_6 > 0$ and red-detuned light $\Delta < 0$, or vice versa. If both C_6 and Δ have the same sign, a resonance appears for the distance at which the energies of the $|gg\rangle$ and $|rr\rangle$ states become equal.

An advantage of Rydberg dressing is the prolonged lifetime of the dressed state compared to the bare Rydberg state's lifetime τ [34]:

$$\tau_{\text{dressed}} = \frac{1}{\beta^2}\tau. \tag{1.10}$$

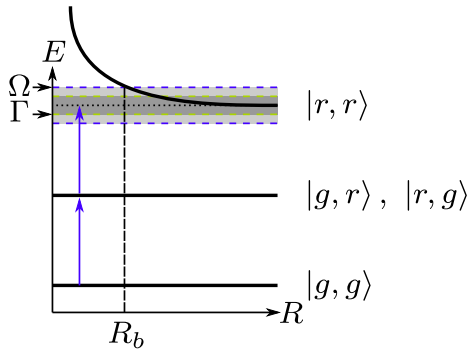

(a) Schematic drawing of the blockade between two Rydberg atoms where the van-der-Waals interaction shifts the doubly excited state out of resonance

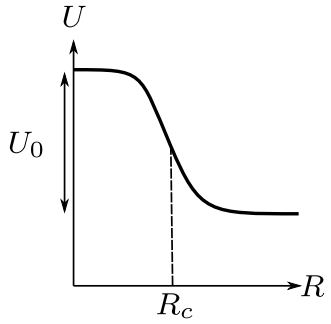

(b) Schematic drawing of the soft-core potential betweeen two Rydberg-dressed atoms

Figure 1.2: Van-der-Waals interaction for resonant Rydberg atoms and soft-core potential for Rydberg-dressed states

The interaction strength between Rydberg-dressed states has a dependency $\propto \Omega^4/\Delta^3$ while the lifetime scales with $\propto \Delta^2/\Omega^2$. This means that in order to achieve long lifetimes while retaining a high interaction strength, we need a high Rabi frequency Ω. In the experiment high Rabi frequencies are achieved by high laser intensities which justifies the need for a high power UV laser source tunable between 285.5 and 288.5 nm corresponding to $N = 20$ to ionization.

As we have seen in this section, alkali atoms are described by a corrected hydrogen atom model. There are different methods to excite a Rydberg level and the resulting lifetime depends strongly on the main quantum number n. Furthermore with Rydberg dressing it is possible to allow for long-range interactions between atoms, which can be implemented in an optical lattice.

2 Theory of Frequency Doubling

The energetic transition to Rydberg states in Potassium corresponds to wavelengths in the UV. For our experiments with Rydberg dressing, we need optical coupling between the atoms and laser light with a wavelength between 285.5 and 288.5 nm. To generate UV light, usually the frequency of a visible laser is doubled. This visible light can be generated directly, e.g. with a dye laser, or in our case be generated by a second doubling from an infrared laser source. The latter approach is chosen here.

We will see that frequency doubling is a non-linear effect in second order of the electric field. To observe these nonlinear optical phenomena, the light field must be coherent and its power sufficiently high, i.e. of the order of the interatomic electric field strength (10^6-10^8 V/m). Lasers can fulfill these requirements for high power and coherence. Indeed, the first demonstration of a working laser in 1960 [36] was quickly followed by the discovery of second harmonic generation [37], marking the beginning of the field of non-linear optics. Due to the presence of light, the optical properties of a material can change and lead to a non-linear behavior. For example, the electric field obtained from second harmonic generation (SHG) scales quadratically with the fundamental light's electric field. The expression for the induced second harmonic electric field is derived in Sec. 2.1. To obtain a non-negligible frequency doubling, a phase matching condition must be fulfilled as we show in Sec. 2.2. We examine second harmonic generation in the case of Gaussian beams in Sec. 2.3 which is of practical relevance for the construction of the two doubling cavities.

2.1 Non-Linearity in Media and Second-Harmonic Generation

It is possible to write a material's response to light in powers of the electric field E. The induced polarization is then [38]:

$$\begin{aligned} P(t) &= \varepsilon_0 \left[\chi^{(1)} E(t) + \chi^{(2)} E^2(t) + \chi^{(3)} E^3(t) + \dots \right] \\ &\equiv \tilde{P}^{(1)}(t) + \tilde{P}^{(2)}(t) + \tilde{P}^{(3)}(t). \end{aligned} \tag{2.1}$$

The first term of the expansion accounts for linear effects and the proportionality factor $\chi^{(1)}$ corresponds to the linear susceptibility. The following two contributions represent second and third order non-linear effects, and define the second and third-order non-linear optical susceptibilities $\chi^{(2)}$ and $\chi^{(3)}$ as well as the respective induced polarizations $\tilde{P}^{(2)}(t)$, $\tilde{P}^{(3)}(t)$. For the occurrence of second order effects $\chi^{(2)} \neq 0$, it is necessary for the medium to be non-centrosymmetric, which excludes liquids and many crystals. However, we choose media for this work which fulfill this criterion and therefore allow to exploit second-order nonlinear effects. Specifically, we use crystals made of Lithium Triborate (LBO) for the first doubling stage and Cesium Lithium Borate (CLBO) for the second.

Second Harmonic Generation (SHG) is a second order effect. It is a special case of the sum-frequency generation, where two light fields of different frequencies yield a third one, the frequency of which corresponds to the sum of the other two. For SHG the frequencies of the two incoming beams are equal. In our setup, this process enables us to double the frequency of our laser source. Considering media for which effects of order higher than two are negligible, the non-linear polarization P_{NL} can be written as:

$$P_{NL} = \chi^{(2)} \varepsilon_0 E(t)^2 = 2 d_{\text{eff}} E(t)^2, \tag{2.2}$$

where d_{eff} is the non-linear coefficient of the medium.

In the following, we derive the formula for the second harmonic electric field. We start with a linear light field propagating along the z-axis [39]:

$$E = \frac{1}{2}\left(\mathcal{E}_\omega(z)e^{-i(\omega t - k_\omega z)} + \mathcal{E}^*_\omega(z)e^{i(\omega t - k_\omega z)}\right), \tag{2.3}$$

where $\mathcal{E}_\omega(z)$ is the electric field's amplitude, ω its frequency and k_ω its wave vector. The corresponding non-linear polarization is:

$$P^{NL}_{2\omega} = \frac{1}{2}d_{\text{eff}}\left(\mathcal{E}^2_\omega(z)e^{-i(2\omega t - 2k_\omega z)} + \mathcal{E}^{*2}_\omega(z)e^{i(2\omega t - 2k_\omega z)}\right). \tag{2.4}$$

This induced polarization radiates an electric field with frequency 2ω:

$$E_{2\omega} = \frac{1}{2}\left(\mathcal{E}_{2\omega}e^{-i(2\omega t - k_{2\omega} z)} + \mathcal{E}^*_{2\omega}e^{i(2\omega t - k_{2\omega} z)}\right). \tag{2.5}$$

In first order this generated electric field induces another contribution to the polarization at 2ω. The total polarization at 2ω is then:

$$P_{2\omega} = \frac{1}{2}\left(\mathcal{P}^{NL}_{2\omega}e^{-i(2\omega t + k_\omega z)} + \mathcal{P}^{L}_{2\omega}e^{-i(2\omega t - k_{2\omega} z)} + c.c.\right), \tag{2.6}$$

where $\mathcal{P}^{NL}_{2\omega}$ and $\mathcal{P}^{L}_{2\omega}$ are the amplitude of the induced non-linear and linear polarization fields. The first term corresponds to the non-linear polarization induced by the original field at ω. The second contribution is the linear polarization induced by the electric field at 2ω which is radiated by the non-linear polarization, i.e. the first term.

Both the polarization and electric field at 2ω must obey the one-dimensional wave equation:

$$\left(\frac{\partial^2}{\partial z^2} - \varepsilon_0\mu_0\frac{\partial^2}{\partial t^2}\right)E_{2\omega} = \mu_0\frac{\partial^2}{\partial t^2}P_{2\omega}. \tag{2.7}$$

To solve eq. 2.7 for $\mathcal{E}_{2\omega}$, the amplitude of the total electric field at 2ω, we use the slowly varying amplitude and phase approximation (SVAPA). In this approximation and by expressing the linear polarization as $\mathcal{P}^L_{2\omega} = \varepsilon\chi^{(1)}_{2\omega}\mathcal{E}_{2\omega}$, we obtain the differential equation:

$$\frac{\partial\mathcal{E}_{2\omega}}{\partial z} = i\omega\frac{\sqrt{\mu_0/\varepsilon_0}}{n_{2\omega}}d_{\text{eff}}\mathcal{E}^2_\omega e^{i\Delta k z}, \tag{2.8}$$

with $\Delta k = 2k_\omega - k_{2\omega}$ the phase mismatch. To better understand the behavior of $\mathcal{E}_{2\omega}$, we solve this differential equation in the simplified case that there is no depletion of the fundamental beam over the length L of the non-linear medium. These assumptions lead to the following electric field amplitude:

$$\mathcal{E}_{2\omega}(z) = i\omega\frac{\sqrt{\mu_0/\varepsilon_0}}{n_{2\omega}}d_{\text{eff}}\mathcal{E}^2_\omega(0)ze^{i\Delta k z/2}\frac{\sin(\Delta k z/2)}{\Delta k z/2}. \tag{2.9}$$

The corresponding intensity after the non-linear medium exhibits the following dependencies:

$$I_{2\omega} \propto I^2_\omega(0)L^2\left(\frac{\sin(\Delta k L/2)}{\Delta k L/2}\right)^2. \tag{2.10}$$

For the intensity of the second harmonic light to be significant, the sinc function must have an argument close to zero. Also, to increase the value of $I_{2\omega}$, the intensity of the incoming beam must be high and the converting medium has to be long. However, we remind ourselves that the solution was obtained without taking into account the depletion of the fundamental beam, which is inaccurate for large L.

2.2 Phase-Matching

As mentioned in the previous section, the value ΔkL must be close to zero for the second harmonic's intensity to be significant. The intensity depends on Δk due to the difference in phase velocity between the two waves. As the first wave travels with a velocity of c/n_ω, the generated contributions to the second harmonic beam travel with a different velocity $c/n_{2\omega}$. This leads to a phase mismatch between the contributions and therefore destructive interference. Quantitatively, this reduction in intensity of the second harmonic wave is contained in the factor $\sin^2(\Delta kL/L)/(\Delta kL/2)^2$, which is a squared sinc function. This function is plotted in Fig. 2.1 and shows that to have a non-negligible second harmonic intensity, the length of the medium must either be of the order of the coherence length L_c or the refractive indices of both waves must be equal, i.e. $\Delta k = 0$. The coherence length L_c of the medium is the length for which the phase of the fundamental beam and the one of the second harmonic light are 180° apart from each other. For this length the function has dropped to 40 % of its maximum value. For commonly used non-linear media it is of the order of 10 µm. However, L appears as a multiplicative factor in Eq. 2.10, therefore using small L also decreases the value of the intensity [40]. Decreasing the non-linear medium's length also decreases the second-harmonic intensity, we must therefore resort to phase-matching.

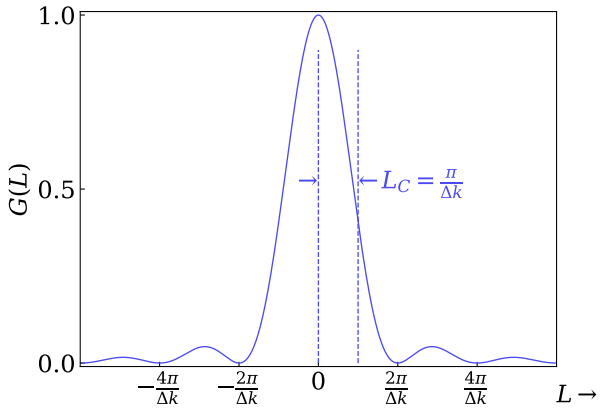

Figure 2.1: Depiction of the phase mismatch factor $G(L) = \sin^2(\alpha L)/(\alpha L)^2$ with $\alpha = \Delta k/2$

Consequently, the condition for a non-negligible second harmonic intensity is:

$$\Delta k = 2k_\omega - k_{2\omega} = 0 \;\Leftrightarrow\; n_{2\omega} = n_\omega. \tag{2.11}$$

Eq. 2.11 is called the phase-matching condition. There are two main possibilities to meet this condition: quasi phase-matching or the use of a birefringent medium.

The first option makes use of a periodically polarized non-linear medium, for which the spatial periodicity is equal to the phase mismatch Δk. The periodicity of the refractive index then compensates the difference in phase velocity of the fundamental and second harmonic light. The non-linearity d_{eff} of the medium is then replaced by:

$$d_{\text{eff}}(z) = \frac{d_0}{2}\left(e^{ik'z} - e^{-ik'z}\right), \tag{2.12}$$

where d_0 is the new non-linearity of the medium and k' the periodicity's wavenumber. Replacing the former d_{eff} in Eq. 2.8 with the periodic one, then leads to the following expression for the

second harmonic electric field:

$$\begin{aligned}\frac{\partial \mathcal{E}_{2\omega}}{\partial z} &= i\omega \frac{\sqrt{\mu_0/\varepsilon_0}}{n_{2\omega}} d_{\text{eff}} \mathcal{E}_\omega^2 \left(e^{i(k'+\Delta k)z} + e^{-i(k'-\Delta k)z} \right) \\ &\overset{k'=\Delta k}{\approx} i\omega \frac{\sqrt{\mu_0/\varepsilon_0}}{n_{2\omega}} \frac{d_0}{2} \mathcal{E}_\omega^2.\end{aligned} \tag{2.13}$$

In the last step, we set Δk and k' equal and disregard the first term which leads to a contribution similar to the one from Eq. 2.9. This new equation for the second harmonic field lacks the exponential dependence on the phase mismatch. Subsequently, the corresponding intensity does not have a squared sinc function dependence on ΔkL, which was responsible for the decrease in intensity. As the phase of the waves is not matched, this method is called quasi phase-matching. As the polarizations of all involved waves are usually parallel, it can also be called type 0 phase matching.

The second possibility for phase matching makes use of the birefringence in certain materials and can be divided into type I and type II phase matching. For type I the two fundamental waves necessary for the new frequency generation have the same polarization. The resulting second harmonic beam then has a polarization orthogonal to the fundamental one. This method is used for both the first and second doubling stages of this work. For type II phase matching the two fundamental waves have orthogonal polarizations.

Type I and type II can further be classified into critical and noncritical phase matching. The first uses the geometric dependence of the refractive index relative to the crystal axis while the second makes use of its temperature dependence. For the first doubling stage, with a LBO crystal and a fundamental wavelength of approximately 1150 nm, it is possible to use non-critical phase matching at a temperature of about 70 °C (the fundamental beam is the extraordinary beam while the generated one is ordinary: $e + e \rightarrow o$). For the second doubling stage, we use critical phase matching, by choosing a crystal axis orientation relative to the propagation direction where $n_{2\omega} = n_\omega$. For CLBO with a fundamental wavelength of 575 nm this corresponds to an angle θ of 54.3° (the fundamental beam is the ordinary beam while the generated one is extraordinary: $o + o \rightarrow e$).

2.3 The Boyd-Kleinman Integral

The light field emitted by lasers is better approximated by Gaussian beams, compared to the plane wave we discussed in the previous Sections. Using Gaussian beams instead of plane waves leads to corrections of our previous result. We will discuss the main steps of the derivation, which lead to the corrected formula for the second harmonic light field. For a more detailed treatment, we refer to the literature [41]. Conceptually, the approach is to divide the crystal into infinitesimally small slices. The contribution to the second harmonic light of a single infinitesimal slice is calculated. To assess the total second harmonic field, these contributions are added up coherently after the crystal on an observation plane, see Fig. 2.2.

In anisotropic media an important effect which has to be taken into account is walkoff. This happens when the beam does not propagate along one of the crystallographic axes. This is the case for the critical phase matched SHG in CLBO. This anisotropy causes the generated second harmonic light in each slice to have a certain angle with regard to the initial beam. On the observation plane where all contributions are added coherently, each second harmonic addition has a different spatial displacement. The resulting beam profile is then no longer Gaussian. An explanatory figure for the walkoff effect is shown in Fig. 2.2.

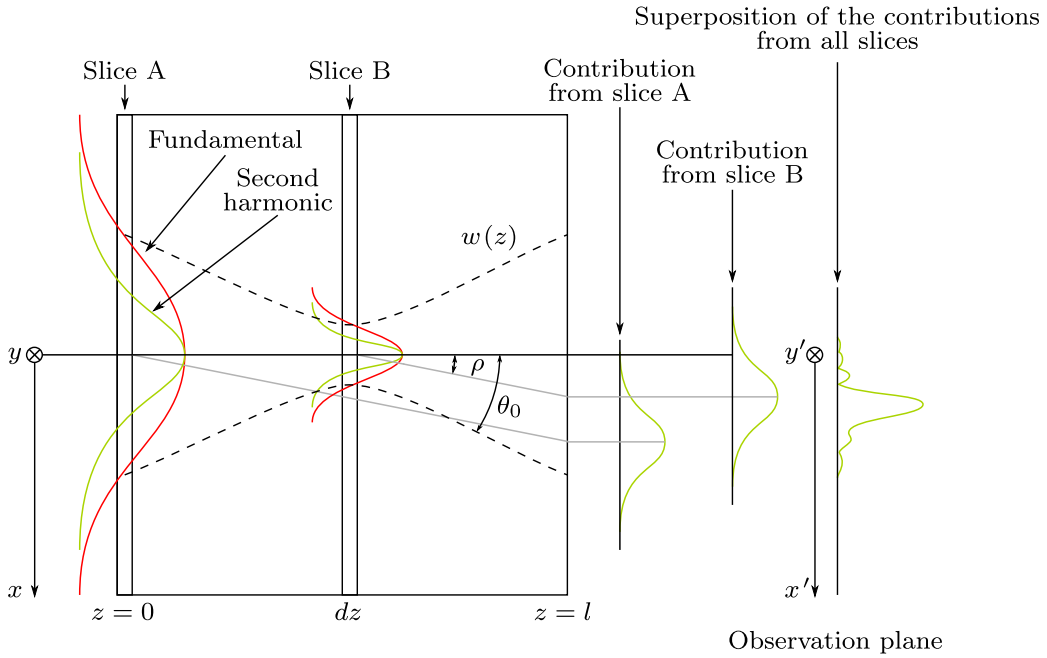

Figure 2.2: Schematic drawing of the walkoff effect in non-linear media with critical phase matching

An important quantity for our setup is the power of the generated second harmonic light. In the following we present the main steps which lead to a formula for the power [42]. We start with a Fourier transformed Gaussian beam (see Sec. 3.2):

$$\mathcal{E}_1(r,z,t) = 2\pi\left[\tilde{E}_1(r,z)\,\delta(\omega-\omega_1) + \tilde{E}_1^*(r,z)\,\delta(\omega+\omega_1)\right], \tag{2.14}$$

where:

$$\tilde{E}_1(r,z) = \frac{E_0}{2}\frac{w_o}{w(z)} e^{-\frac{\alpha_1}{2}z} e^{-\frac{r^2}{w^2(z)}} e^{-ik_z} e^{\frac{ikr^2}{2R(z)}} e^{i\phi(z)}, \tag{2.15}$$

with α_1 the absorption coefficient of the fundamental beam and the functions $\phi(z)$, $w(z)$, $R(z)$ are defined in Sec. 2.2. The minimum waist of the Gaussian beam in Eq. 2.14 is located at $z=0$. To obtain a more general expression, we shift the position to $z=f$ and introduce the notation $\zeta = {}^{2(z-f)}/_{b}$, with $b = 2z_r = {}^{2\lambda}/_{\pi n w_0^2}$. The electric field can then be written as:

$$\tilde{E}_1(r,z) = \frac{E_0}{2} e^{-\frac{\alpha_1}{2}z} \frac{1}{1+i\zeta} e^{-\frac{2r^2}{w_0^2(1+i\zeta)}} e^{-ik_1 z}. \tag{2.16}$$

The second order induced polarization is then:

$$\tilde{P}^{(\omega_3)} = 2\varepsilon d_{\text{eff}}\left[\tilde{E}^{(\omega_1)}\right]^2 = \varepsilon_0 d_{\text{eff}} \frac{E_0^2}{2} e^{-\alpha_1 z}\left(\frac{1}{1+i\zeta}\right)^2 e^{-\frac{2r^2}{w_0^2(1+i\zeta)}} e^{-2ik_1 z}. \tag{2.17}$$

Analogously to Eq. 2.8, we calculate the electric field generated by the polarization in a slice dz of the crystal and obtain:

$$\begin{aligned} d\tilde{E}_3(x) &= -\frac{i}{2\varepsilon_0 n_3^2} k_3 e^{ik_3 z}\tilde{P}^{(\omega_3)}\,dz \\ &= -\frac{ik_3}{2n_3^2} e^{i\Delta k z} d_{\text{eff}} \frac{E_0^2}{2} e^{-\alpha_1 z} \frac{1}{1+i\zeta}\left\{\frac{1}{1+i\zeta} e^{-\frac{2r^2}{w_0^2(1+i\zeta)}}\right\} dz. \end{aligned} \tag{2.18}$$

The expression in the braces resembles a Gaussian beam with beam waist $w_0/\sqrt{2}$, confocal parameter b and focus at $z = f$.

The crystal slab dz at (x, y) contributes, due to a walkoff angle ρ in the xz-plane to the field at a point x', y' and z' outside of the crystal. For this observation point, the coordinates are in a small-angle approximation $x' = x + \rho\,(l - z)$, $y' = y$ and $\zeta' = 2(z'-f)/b$. This propagation can be expressed in the Gaussian part of Eq. 2.18 by replacing the original coordinate with x', y' and z'. We then integrate over all z-contributions along the crystal length l and obtain:

$$\tilde{E}_3\left(r', z'\right) = -\frac{ik_3}{2n_3^2} d_{\text{eff}} \frac{E_0^2}{2} e^{-\frac{\alpha_3}{2} l} \int_0^l \frac{e^{-\alpha z} e^{i\Delta k z}}{1 + i\zeta} \left\{ \frac{1}{1 + i\zeta'} e^{-\frac{2\left\{[x' - \rho(l-z)]^2 + [y']^2\right\}}{w_0^2 (1 + i\zeta')}} \right\} dz, \tag{2.19}$$

where $\alpha = \alpha_1 - \alpha_3/2$ and α_3 takes into account the loss of the second harmonic light in the medium. To simplify the expression, we introduce normalized spatial coordinates:

$$\begin{aligned} u &= \frac{x' - \rho\left(l - f\right)}{w_0 \zeta'} \\ v &= \frac{y'}{w_0 \zeta'} \\ \beta &= \frac{\rho}{\theta_0} \end{aligned} \tag{2.20}$$

and let $\zeta' \to \infty$ for an observation point at infinite distance. The electric field then simplifies to:

$$\tilde{E}_3\left(r', z'\right) = -\frac{k_3}{2n_3^2} d_{\text{eff}} \frac{E_0^2}{2\zeta'} e^{-2(1 - i\zeta')(u^2 + v^2)} \int_0^l \frac{e^{-\alpha z} e^{i\Delta k z} e^{4iu\beta\zeta}}{1 + i\zeta} dz. \tag{2.21}$$

To conform to the notation in [41], we define the following variables:

$$\begin{aligned} \kappa &= \frac{\alpha b}{2} \\ \sigma &= \frac{\Delta k b}{2} \\ \mu &= \frac{l - 2f}{l} \\ \xi &= \frac{l}{b}, \end{aligned} \tag{2.22}$$

make the substitution $\zeta = 2(z-f)/2$ and define the integral:

$$H\left(\sigma + 4\beta\mu, \kappa, \xi, \mu\right) = \frac{1}{2\pi} \int_{-\xi(1-\mu)}^{\xi(1+\mu)} \frac{e^{-\kappa\zeta} e^{i(\sigma + 4\beta\mu)\zeta}}{1 + i\zeta} d\zeta. \tag{2.23}$$

In this new representation, the electric field reads:

$$\tilde{E}_3\left(r', z'\right) = \frac{-k_3}{2n_3} d_{\text{eff}} \frac{E_0^2}{2\zeta'} e^{-\alpha_3 l/2} e^{-2(1 - i\zeta')(u^2 + v^2)} \frac{b}{2} e^{-\alpha f} e^{i\Delta k f} \left[2\pi H\left(\sigma + 4\beta\mu, \kappa, \xi, \mu\right)\right]. \tag{2.24}$$

We integrate the corresponding intensity over the dimensions u and v and obtain an expression for the second harmonic power:

$$P_3 = \underbrace{\frac{16\pi^2 d_{eff}^2}{\varepsilon_0 c \lambda_1^3 n_3 n_1} P_1^2 e^{-\alpha' l} l}_{\kappa_{NL}} h\left(\sigma, \beta, \kappa, \xi, \mu\right), \tag{2.25}$$

with P_1 the power of the fundamental beam, $\alpha' = \alpha_1 + \alpha_3/2$ and the Boyd-Kleinman factor:

$$h(\sigma,\beta,\kappa,\xi,\mu) = \frac{2\pi^{3/2}}{\xi} e^{\mu\alpha l} \int_{-\infty}^{+\infty} du e^{-4u^2} \left| H(\sigma + 4\beta u,\kappa,\xi,\mu) \right|^2 . \tag{2.26}$$

Eq. 2.25 shows the strong dependence of the second harmonic's power on the power of the fundamental beam and the nonlinearity of the medium. Both quantities appear quadratically in the formula. For practical purposes the Boyd-Kleinman factor is further simplified in Sec. 5.1.

In this section we discussed the emergence of non-linear optics in the particular case of second harmonic generation. We have showed the necessity of phase matching for SHG and described different possibilities to achieve it. For the construction of the cavities we looked into the second harmonic conversion of Gaussian beams and derived the resulting power. We will in Chapter 5 use this formula to calculate a geometry for the doubling cavities so that the second harmonic power is maximized.

3 Optical Resonators

In this work, we need optical resonators for two purposes, cavity-enhanced second harmonic generation and frequency stabilization of a laser using a reference cavity. They are alignments of two or more mirrors. Their geometric configuration allows for the formation of a standing or traveling wave of the incoupled light. Optical resonators play an important role in the construction of lasers as they surround the gain medium and provide feedback on the laser light.
In order to understand how the light couples into an optical resonator, we first look at the geometric ray approach of optics and then move on to a more realistic description of light, provided by Gaussian beams. Subsequently, we describe the specific resonators used in this thesis. Finally, we establish the characteristic values of resonators and define a condition for impedance matching for one of the thesis' cavities.

3.1 Cavity Matrices and Stability

Geometric optics assumes the light to propagate as rays. The direction of propagation is assumed to be perpendicular to the wavefronts and the width of the beam is negelected in this approach [40]. A beam traveling in the xy-plane and forming only a small angle with the z-axis can be described by a vector with two components. The first entry is the lateral displacement $r(z)$ and the second the slope $r'(z)$ with respect to the z-axis. From the roughly unidirectional propagation along z, we can use the small-angle approximation, such that:

$$r'(z) = \frac{dr}{dz} = \tan(\theta) \approx \sin(\theta) \approx \theta. \tag{3.1}$$

This vector description characterizes paraxial rays. In this notation the effect of optical elements as well as the propagation of the ray are expressed by matrices. The matrices for the optical resonators which are for interest to this thesis are listed in Tab. 1 [43].

Optical Element	**Corresponding Matrix**
Propagation through a homogeneous medium of length d	$\begin{pmatrix} 1 & d \\ 0 & 1 \end{pmatrix}$
Refraction at a dielectric interface from a medium with refractive index n_1 to another with n_2	$\begin{pmatrix} 1 & 0 \\ 0 & n_1/n_2 \end{pmatrix}$
Reflection at a spherical mirror with a radius of curvature R	$\begin{pmatrix} 1 & 0 \\ -2/R & 1 \end{pmatrix}$

Table 1: Ray transfer matrices for the optical elements relevant for this thesis

To find the displacement and slope after an optical element described by the matrix M, we have to evaluate the following vector-matrix product:

$$\begin{pmatrix} r_f \\ r'_f \end{pmatrix} = M \cdot \begin{pmatrix} r_i \\ r'_i \end{pmatrix}, \tag{3.2}$$

where $\left(r_{i,f}, r'_{i,f}\right)^T$ are the initial and final vectors respectively. The effect of several consecutive elements M_1, M_2, M_3 is therefore captured by their matrix product, i.e. $M_{tot} = M_3 \cdot M_2 \cdot M_1$.

The ray transfer matrices from Tab. 1 suffice to describe the cavities used in this thesis. However, not all assemblies of mirrors are stable resonators. In the following we show that a stability condition has to be fulfilled for the resonator to retain the light. We start by assuming a cavity described by the four matrices M_1, M_2, M_3, M_4. The corresponding roundtrip through the resonator can therefore be expressed by the matrix $M = M_4 \cdot M_3 \cdot M_2 \cdot M_1$. The light will pass through the resonator several times and the matrix describing the ray transfer after the n^{th} roundtrip is therefore the n^{th} power of M. We rewrite the resulting matrix with Sylvester's theorem which yields [44][45]:

$$M^n = \begin{pmatrix} A & B \\ C & D \end{pmatrix}^n = \frac{1}{\sin(\theta)} \begin{pmatrix} A\sin(n\theta) - \sin((n-1)\theta) & B\sin(\theta) \\ C\sin(n\theta) & D\sin(n\theta) - \sin((n-1)\theta) \end{pmatrix}, \tag{3.3}$$

where the angle θ is defined as:

$$\cos(\theta) = \frac{1}{2}(A+D). \tag{3.4}$$

Motivated by this definition we distinguish two cases. The first case is:

$$\frac{1}{2}(A+D) < -1 \ \wedge \ 1 < \frac{1}{2}(A+D), \tag{3.5}$$

which leads to hyberbolic functions in Eq. 3.3 and therefore to diverging entries of the matrix for large n. In terms of the ray in the resonator: with each roundtrip the resulting ray vector grows and eventually diverges. This behavior corresponds to an unstable resonator. On the other hand the second case, for which:

$$-1 < \frac{1}{2}(A+D) < 1, \tag{3.6}$$

allows for a bounded ray transfer matrix for large n and corresponds to a periodic refocusing of the ray. Eq. 3.6 is also called stability condition.
For the construction of cavities it is therefore necessary to restrict the cavity parameters to stable solutions for which the rays are periodically refocused.

3.2 Gaussian Beams and ABCD Law

The description of beams by ray optics enables us to formulate a stability condition for resonators. However, this description is not sufficient as it cannot describe the incoupling of light or resonator modes. We therefore extend the description from rays to Gaussian beams. In the following, we derive the formula for a Gaussian beam. We start with the wave equation from Maxwell's equations under the condition of no currents and a charge-free and non-magnetic material [40]:

$$\nabla^2 E(\boldsymbol{r}, t) = \frac{1}{c^2} \frac{\partial^2 E(\boldsymbol{r}, t)}{\partial t^2}. \tag{3.7}$$

For a monochromatic field, of the form:

$$E(\boldsymbol{r}, t) = \mathcal{E}(\boldsymbol{r})\, e^{-i\omega t}, \tag{3.8}$$

the wave equation can be rewritten to the Helmholtz equation:

$$\nabla^2 \mathcal{E}(\boldsymbol{r}) + k^2 \mathcal{E}(\boldsymbol{r}) = 0. \tag{3.9}$$

An ansatz for the solution to the Helmholtz equation is to add a finite cross section to a plane wave. The general form of this ansatz is:

$$\mathcal{E}(\boldsymbol{r}) = \mathcal{E}_0(\boldsymbol{r})\, e^{-ikz}. \tag{3.10}$$

In a slowly varying amplitude approximation, this solution must fulfill the paraxial approximation of the wave equation:

$$\nabla_T^2 \mathcal{E}_0 + 2ik\frac{\partial \mathcal{E}_0}{\partial z} = 0. \tag{3.11}$$

A solution to this approximated wave equation is the Gaussian beam:

$$\mathcal{E}(\boldsymbol{r}) = A\frac{w_0}{w(z)} e^{-ikz} e^{-i\phi(z)} e^{ik(x^2+y^2)/2R(z)} e^{-(x^2+y^2)/w^2(z)}, \tag{3.12}$$

where A is a constant, w_0 the minimum beam waist, $w(z) = w_0\sqrt{1+z^2/z_0^2}$ the waist, $z_0 = \pi w_0^2/\lambda$ the Rayleigh range, $R(z) = z + z_0^2/z$ the radius of curvature and $\phi(z) = \arctan(z/z_0)$ the Gouy phase. The angle $\theta = \lambda/\pi n w_0$ is the divergence of the beam. Another parameter important for later descriptions is the q-parameter: $1/q(z) = 1/R(z) + i\lambda/\pi w^2(z)$. An illustration of the Gaussian beam with its relevant parameters is shown in Fig. 3.1.

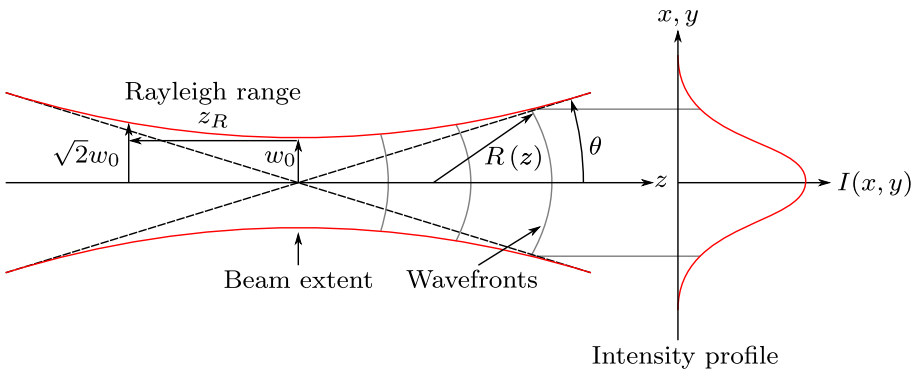

Figure 3.1: Illustration of a Gaussian beam with a minimum beam waist w_0, a Rayleigh range z_R, a beam curvature $R(z)$ and a divergence θ. On the right is depicted the Gaussian intensity profile of the beam, the waist $w(z)$ corresponds to the distance for which the intensity has dropped to $1/e^2$ of its maximum value

For the construction of cavities, it is necessary to describe the effect of optical components on Gaussian beams. The ABCD law uses the matrices from ray optics to evaluate the transformation of Gaussian beams sent through an optical system by transforming the q-parameter in the following way:

$$q_f = \frac{Aq_i + B}{Cq_i + D}, \tag{3.13}$$

where q_i denotes the q-parameter of the initial beam and q_f of the final one after the optical component characterized by a matrix with coefficients A, B, C, D.
Consequently, in order to obtain a Gaussian mode inside a resonator, the q-parameter must not change after one roundtrip. With the ABCD law from Eq. 3.13, the condition for a Gaussian beam mode becomes:

$$q(z) = \frac{Aq(z) + B}{Cq(z) + D}, \tag{3.14}$$

where A, B, C, D describe the optical system made up of a resonator and $q(z)$ the beam's q-parameter at an arbitrary point z in the cavity. Solving for the roots of q with the characteristic of these ray matrices that $AD - BC = 1$ leads to two solutions:

$$q = \frac{D-A}{2B} \overset{(+)}{(-)} \frac{i}{2B}\sqrt{4-(A+D)^2}. \tag{3.15}$$

This corresponds to the self-consistency condition for a Gaussian beam and is used for the parameter optimization of the bow-tie cavities in Sec. 5.
For bow-tie cavities such as the one shown in Fig. 3.2b, the angle of incidence of the beam is non-zero. Therefore, some of the matrices from Sec. 3.1 must be corrected. We distinguish between a tangential and sagittal plane. The first is parallel to the plane of incidence while the second is perpendicular to it. The optical elements which are affected by this correction are the refraction at a dielectric medium and the reflection at a curved interface. For the first, we restrict ourselves to refraction at an interface cut in a Brewster angle, as this is the relevant case for our bow-tie cavity with the Brewster cut crystal (Fig. 3.2b). The resulting corrected matrices are shown in Tab. 2. For the Gaussian beam, this means that we must distinguish between the two planes. We will obtain slightly different Gaussian beams whether we place ourselves in the sagittal or tangential plane.
With the self-consistency condition for Gaussian beams in a resonator and the corrected matrices, it is possible to accurately describe the beam inside the resonators of interest to this thesis.

Optical Process	**Plane**	**Corresponding Matrix**
Refraction at an interface at a Brewster angle from a medium with refractive index n_1 to another with n_2	Tangential plane	$\begin{pmatrix} n_2/n_1 & 0 \\ 0 & (n_1/n_2)^2 \end{pmatrix}$
	Sagittal plane	$\begin{pmatrix} 1 & 0 \\ 0 & n_1/n_2 \end{pmatrix}$
Reflection at a spherical mirror with a radius of curvature R and an angle of incidence θ	Tangential plane	$\begin{pmatrix} 1 & 0 \\ -2/R\cos(\theta) & 1 \end{pmatrix}$
	Sagittal plane	$\begin{pmatrix} 1 & 0 \\ -2\cos(\theta)/R & 1 \end{pmatrix}$

Table 2: Ray transfer matrices for optical elements with corrections due to a non-zero angle of incidence [46]

3.3 Hemispherical and Bow-Tie Cavity

Two cavities are used in this thesis. The first is is a hemispherical cavity made of Ultra Low Expansion glass and is used for the frequency stabilization of the infrared laser. The second one is a bow-tie cavity and is used for the two frequency doubling stages from the infrared to the green and finally ultraviolet. It is needed to enhance the power of the fundamental beam and increase the conversion efficiency of the non-linear medium, i.e. the crystal placed inside it.

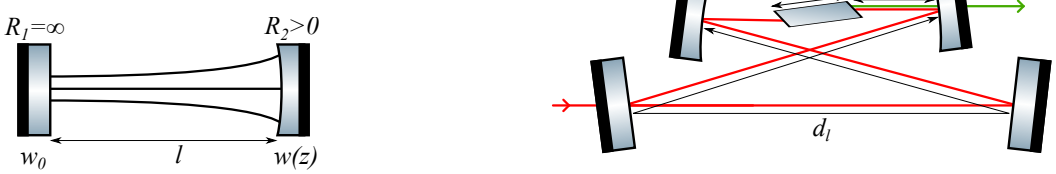

(a) Hemispherical Cavity

(b) Bow-Tie Cavity with a Brewster-cut crystal

Figure 3.2: Resonators used in this thesis

Hemispherical Cavity

A hemispherical cavity is made up of one concave and one plane mirror. This configuration is shown in Fig. 3.2a. The distance between the mirrors is set by the length l of the cavity, which in this thesis corresponds to the Ultra Low Expansion (ULE) Cavity manufactured by Advanced Thin Films. In the following, we verify the stability of our hemispherical cavity and determine parameters which must apply to the beam to be incoupled. The matrix describing this cavity is:

$$M = \underbrace{\begin{pmatrix} 1 & 0 \\ -2/R_1 & 1 \end{pmatrix}}_{R_1 \to \infty} \cdot \begin{pmatrix} 1 & l \\ 0 & 1 \end{pmatrix} \cdot \underbrace{\begin{pmatrix} 1 & 0 \\ -2/R_2 & 1 \end{pmatrix}}_{R_2 > 0} \cdot \begin{pmatrix} 1 & l \\ 0 & 1 \end{pmatrix}, \tag{3.16}$$

where R_1 and R_2 are the radii of curvature of the two mirrors. With the condition in Eq. 3.6, it is possible to determine for which values of l, R_1 and R_2 the resonator is stable. For the general case of a two mirror resonator, which applies to our hemispherical cavity, the stability condition simplifies to:

$$\begin{aligned} 0 < \left(1 - \frac{l}{R_1}\right) \cdot \left(1 - \frac{l}{R_2}\right) < 1 \\ \Leftrightarrow 0 < g_1 \cdot g_2 < 1, \end{aligned} \tag{3.17}$$

with $g_{1,2} = 1 - l/R_{1,2}$. For our hemispherical resonator, $R_1 \to \infty$ and $R_2 > 0$, therefore, this condition is fulfilled as long as $l < R_2$. This is the case for the mirrors in our ULE cavity for which $l = 10\,\text{cm}$ and $R_2 = 50\,\text{cm}$. The stability diagram for a two-mirror resonator is shown in Fig. 3.3. In this Figure, we depict the stability of our ULE cavity with a red marker relative to other two-mirror resonators.

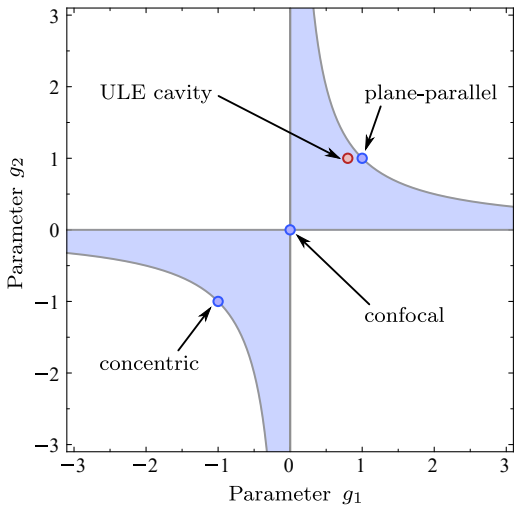

Figure 3.3: Stability diagram of a two-mirror resonator for the parameters $g_1 = 1 - l/R_1$ and $g_2 = 1 - l/R_2$: the stable regions are shown in blue and the red point indicates where the ULE cavity, used in this thesis, is situated

Another important criterion for the incoupling into the cavity is the self-consistency condition for a Gaussian beam in Eq. 3.14. From the cavity matrix, we determine parameters which must apply to the beam to match the Gaussian cavity mode, a procedure called mode-matching. The order of the matrices in Eq. 3.16 sets the position in the resonator, at which the q-parameter is

being calculated. In Eq. 3.16, the last matrix is the one representing the first mirror. Therefore, with this order of matrices, we evaluate the q-parameter at the position of the first plane mirror. Solving for the real part in Eq. 3.15, leads to the curvature the beam must have at this point:

$$\frac{1}{R(0)} = \frac{1}{R_1}. \tag{3.18}$$

Performing two cyclic permutations of the matrices in Eq. 3.16, we now evaluate the q-parameter at the position of the second mirror. Repeating the same procedure as for the first mirror, leads to a second condition for the incoupled beam:

$$\frac{1}{R(l)} = \frac{1}{R_2}. \tag{3.19}$$

The two preceding equations are sufficient to characterize the beam. For a hemispherical resonator, as $R_1 \to \infty$, the first equation gives the position where the beam curvature is infinite and therefore sets the position of the minimum waist w_0 at $z = 0$. The second equation sets the curvature of the beam to R_2 at the position of the second mirror $z = l$. Inserted into the formula for the beam curvature $R(l) = l + z_0^2/l^2$, the resulting Rayleigh range can be rewritten into an equation for the minimum beam waist:

$$w_0 = \sqrt{\frac{\lambda}{\pi}\sqrt{l\,(R_2 - l)}}. \tag{3.20}$$

With Eq. 3.18 and 3.20, we know both the position and value for the minimum beam waist. Thus, we have enough information to couple the infrared laser beam to the Gaussian mode of our ULE cavity.

Bow-Tie Cavity

The bow-tie cavities in this work are used for cavity-enhanced second harmonic conversion. This means that we place a crystal as a non-linear medium in the resonator, which generates second harmonic light. We then use the high circulating powers inside the resonator to achieve a high conversion efficiency.
The bow-tie cavity configuration is shown in Fig. 3.2b. In the most simple configuration, a bow-tie cavity is composed of two plane and two concave mirrors. The beam enters the cavity through one of the plane mirrors and continues to the second plane mirror. Because of a non-zero opening angle, it is deflected to one of the curved mirrors. From there the path continues to the second curved mirror. Finally, it is deflected back to the first mirror, closing the beam path. The crystal is placed midway between the two curved mirrors. The length l denotes the distance traveled inside the crystal. The long arm d_l corresponds to the entire beam path except for the segment between the curved mirrors. The short arm d_s denotes the remaining beam path, that means the path between the curved mirrors except for the segment inside the crystal.
The matrix for this cavity is slightly more complicated than for the hemispherical resonator. Neglecting astigmatism effects, the roundtrip matrix is:

$$\begin{aligned} M &= \begin{pmatrix} 1 & l/2 \\ 0 & 1 \end{pmatrix} \cdot \begin{pmatrix} 1 & 0 \\ 0 & n_1/n_2 \end{pmatrix} \cdot \begin{pmatrix} 1 & d_s/2 \\ 0 & 1 \end{pmatrix} \cdot \begin{pmatrix} 1 & 0 \\ -2/R & 1 \end{pmatrix} \cdot \begin{pmatrix} 1 & d_l \\ 0 & 1 \end{pmatrix} \cdot \begin{pmatrix} 1 & 0 \\ -2/R & 1 \end{pmatrix} \cdot \begin{pmatrix} 1 & d_s/2 \\ 0 & 1 \end{pmatrix} \cdot \begin{pmatrix} 1 & 0 \\ 0 & n_2/n_1 \end{pmatrix} \cdot \begin{pmatrix} 1 & l/2 \\ 0 & 1 \end{pmatrix} \\ &= \begin{pmatrix} 2\gamma_1\gamma_2 - 1 & R\gamma_1\left(1 - \gamma_1\gamma_2\right) \\ -4\gamma_2/r & 2\gamma_1\gamma_2 - 1 \end{pmatrix} \end{aligned}, \tag{3.21}$$

where n_1 is the refractive index of air, n_2 the one of the crystal, R the radius of curvature of the two concave mirrors and we introduced the notation:

$$\begin{aligned}\gamma_1 &:= \frac{-l - n_2/n_1\,(d_s - R)}{R} \\ \gamma_2 &:= \frac{n_1}{n_2}\left(1 - \frac{d_l}{R}\right).\end{aligned} \tag{3.22}$$

The waist inside the crystal is set by the optimization of the Boyd-Kleinman integral, see Sec. 5.1. The remaining geometric parameters which must be determined are the curvature of two of the mirrors R, the length of the short and long arm d_s, d_l, and the opening angle θ. Two requirements allow us to determine these parameters: the stability of the resonator and the self-consistency for a Gaussian beam inside it.
With the order of the matrices in Eq. 3.21 we evaluate the q-parameter in the middle of the crystal, where the waist is minimal and determined by the optimization of the Boyd-Kleinman integral. The stability of this resonator is, as for the hemispherical cavity, set by the inequality of Eq. 3.6. With the compact notation from Eq. 3.22, this condition can be rewritten as:

$$0 < \gamma_1 \cdot \gamma_2 < 1. \tag{3.23}$$

Also, the condition for a Gaussian mode in the resonator from Eq. 3.15 can be solved for the waist inside the crystal. This waist is the minimal waist of the beam. Therefore the curvature must be infinite and $D = A$. The q-parameter then becomes a purely imaginary number:

$$\frac{1}{q} = -\frac{i}{B}\sqrt{1 - A^2}. \tag{3.24}$$

With the definition for the q-parameter, this formula can be further rewritten as:

$$q = \frac{i\pi w_0^2 n_2}{\lambda} = \frac{iR}{2}\sqrt{\frac{\gamma_1}{\gamma_2}\left(1 - \gamma_1\gamma_2\right)}. \tag{3.25}$$

Using the notation from Sec. 2.3 with $\xi = l/b = l/2z_R$ where $z_R = \pi n_2 w_0^2/\lambda$ is the Rayleigh range, it is now possible to define a parameter α in the following way:

$$\alpha^2 = \left(\frac{\xi R}{l}\right)^2 = \frac{\gamma_2}{\gamma_1\left(1 - \gamma_1\gamma_2\right)}. \tag{3.26}$$

This equation characterizes a parametric curve within the stability region for which each point represents a possible self-consistent solution. We now choose a point which is well within the stability region whilst still being on the curve defined by Eq. 3.26. One possibility is to take the minimum of the function. This corresponds to the following values for γ_1 and γ_2:

$$\begin{aligned}\gamma_1 &= -\frac{1}{\alpha} \\ \gamma_2 &= -\frac{\alpha}{2}.\end{aligned} \tag{3.27}$$

With the definition for γ_1 and γ_2 it is now possible to calculate the ensuing values for the short and long arms d_s and d_l:

$$\begin{aligned}d_s &= R\left(1 + \frac{n_1}{n_2}\frac{1}{\alpha}\right) - \frac{n_1}{n_2}l \\ d_l &= R\left(1 + \frac{n_2}{n_1}\frac{\alpha}{2}\right).\end{aligned} \tag{3.28}$$

These values for d_s and d_l are obtained without taking into consideration the astigmatism caused by the curved mirrors and the shape of the crystal. To account for the arising difference between the sagittal and tangential plane caused by the astigmatism, we need to correct some of the matrices in Eq. 3.21. The impacted matrices are the one describing the reflection at a curved mirror and the one for the refraction at a dielectric interface. They need to be replaced by the matrices from Tab. 2.

3.4 Impedance Matching and Finesse

We use the bow-tie cavity configuration for cavity-enhanced second harmonic generation. The circulating power of the light inside the cavity can be reduced by factors such as imperfectly reflecting mirrors. By minimizing these losses inside the resonator, we maximize the second harmonic conversion inside the non-linear crystal. We discuss finesse and free spectral range as the values characterizing any resonator. Then, we derive a condition for a maximized circulating power in a bow-tie resonator.
For the general case, the requirement for a standing wave inside a resonator is an infinite number of waves with equal phase and amplitudes that decrease geometrically by a factor p after each roundtrip. The total amplitude U then amounts to [47]:

$$\begin{aligned} U &= U_1 + U_2 + U_3 + ... \\ &= \sqrt{I_0}\left(1 + p + p^2 ...\right) \\ &= \frac{\sqrt{I_0}}{1-p}, \end{aligned} \tag{3.29}$$

where U_i is the amplitude of the consecutive waves. The factor p accounts for both the losses during a roundtrip as well as the accumulated phase and is therefore of the form $p = re^{i\phi}$. We introduce the factor r, called reflectivity, which for $r < 1 \in \mathbb{R}_+$, accounts for dampening of the waves. The angle ϕ represents the accumulated phase, which we assume to be constant between consecutive waves. The resulting intensity is:

$$\begin{aligned} I = |U|^2 &= \frac{I_0}{\left(1-r^2\right) + 4r\sin^2\left(\frac{\phi}{2}\right)} \\ &= \frac{I_{max}}{1 + \frac{4r}{\left(1-r^2\right)\sin^2\left(\frac{\phi}{2}\right)}}, \end{aligned} \tag{3.30}$$

where we used $I_{max} = {}^{I_0}/_{(1-r^2)}$, the maximum intensity in the case of purely constructive interference, i.e. $\phi = 0$. Further useful definitions are the free spectral range ν_F and the finesse $\mathcal{F}$:

$$\begin{aligned} \nu_F &= \frac{c}{2d} \\ \mathcal{F} &= \frac{\pi\sqrt{r}}{1-r}, \end{aligned} \tag{3.31}$$

where d corresponds to the distance between the two mirrors of a two-mirror resonator. For a bow-tie cavity $2d$ is replaced by the length of a whole roundtrip. With the phase described by $\phi = k \cdot 2d = {}^{4\pi\nu d}/_{\nu_F} = 2\pi{}^{\nu}/_{\nu_F}$, the intensity can be rewritten as:

$$I(\nu) = \frac{I_{max}}{1 + \frac{4\mathcal{F}^2}{\pi^2}\sin^2\left(\frac{\pi\nu}{\nu_F}\right)}, \tag{3.32}$$

a Lorentzian distribution for which the peaks occur at frequencies which are integer multiples of the free spectral range ν_F. The full width at half maximum (FWHM) of these peaks, also referred to as the linewidth, is of the form:

$$\begin{aligned} \delta\nu &= \frac{2\nu_F}{\pi}\arcsin\left(\frac{\pi}{2\mathcal{F}}\right) \approx \frac{\nu_F}{\mathcal{F}} \\ \Leftrightarrow \mathcal{F} &= \frac{\nu_F}{\delta\nu}. \end{aligned} \tag{3.33}$$

The ratio of peak separation to peak width for values of ν close to the peak is therefore determined by the reflectivity of the mirrors. The resulting transmission of a cavity is:

$$\mathcal{T}(\nu) = \frac{I_{trans}(\nu)}{I_{inc}}, \tag{3.34}$$

where the incoming intensity is given by the intensity of the initial wave through $I_0 = |t_1|^2 I_{inc}$ with $|t_1|^2$ being the transmission of the incoupling mirror. The transmitted intensity for a two-mirror resonator is defined by the transmission of the second mirror through $I_{trans} = |t_2|^2 I_{circ} = |t_2|^2 I(\nu)$, where $|t_2|^2$ is the transmission of the second mirror and I_{circ} the circulating intensity. The transmission coefficient is expressed in cavity parameters as:

$$\mathcal{T}(\nu) = \frac{\mathcal{T}_{max}}{1 + \frac{4\mathcal{F}^2}{\pi^2}\sin^2\left(\frac{\pi\nu}{\nu_F}\right)}, \tag{3.35}$$

with the maximum possible transmission $\mathcal{T} = {}^{|t|^2}/_{(1-r)^2}$ and $t = t_1 t_2$ the total transmission of the two mirrors.

We now focus on the circulating power, in the general case of any enhancement cavity. We start with the circulating electric field:

$$\mathcal{E}_{circ} = i\sqrt{T_1}\mathcal{E}_{inc} + g_{rt}(\omega)\,\mathcal{E}_{circ}, \tag{3.36}$$

where the first contribution comes from the incoupling into the cavity with T_1 the transmission power of the first mirror and the second term takes into account phase shifts and losses inside the cavity through the function $g_{rt}(\omega)$. The phase difference of $\pi/2$ due to the incoupling is accounted for by the imaginary factor. The roundtrip function $g_{rt}(\omega)$ is then of the form:

$$g_{rt}(\omega) = \sqrt{\mathcal{R}_N}e^{-i\omega l_N/c}\sqrt{\mathcal{R}_{N-1}}e^{-i\omega l_{N-1}/c}...\sqrt{\mathcal{R}_1}e^{-i\omega l_1/c}\sqrt{\alpha} = \sqrt{\mathcal{R}\alpha}e^{-i\omega l/c}, \tag{3.37}$$

with l_i being the optical lengths between the mirrors, $l = \sum_{i=1}^{N} l_i$ the sum of all lengths, $\mathcal{R}_i$ the reflection power of the mirrors, $\mathcal{R} = \prod_{i=1}^{N}\mathcal{R}_i$ the total reflection and α a loss coefficient for all losses not taken into account by the finite reflection of the mirrors. We are interested in the circulating power with respect to the incoming power:

$$\frac{P_{circ}}{P_{inc}} = \left|\frac{\mathcal{E}_{circ}}{\mathcal{E}_{inc}}\right|^2 = \left|\frac{i\sqrt{T_1}}{1 - g_{rt}(\omega)}\right|^2. \tag{3.38}$$

To maximize the fraction in Eq. 3.38, $g_{rt}(\omega)$ must also be maximized. The maxima of the roundtrip function occur periodically for frequencies which are a multiple of the resonator frequencies $\omega_m = m \cdot \frac{2\pi c}{l}$ with $m \in \mathbb{Z}$. The power enhancement at these maxima then becomes:

$$\left.\frac{P_{circ}}{P_{inc}}\right|_{\omega=\omega_m} = \frac{T_1}{\left(1 - \sqrt{\mathcal{R}\alpha}\right)^2}. \tag{3.39}$$

If the reflected field is minimized, the circulating power is maximized due to energy conservation. The value of the reflected field consists of the portion reflected at the incoupling mirror before the cavity and the part transmitted through the same mirror leaving the cavity, leading to a factor $\sqrt{T_1/\mathcal{R}_1}$:

$$\mathcal{E}_{refl} = \sqrt{\mathcal{R}_1}\mathcal{E}_{inc} + i\sqrt{T_1}\frac{g_{rt}(\omega)}{\sqrt{\mathcal{R}_1}}\mathcal{E}_{circ}. \tag{3.40}$$

The portion of the reflected field is therefore:

$$\frac{\mathcal{E}_{refl}}{\mathcal{E}_{inc}} = \frac{\mathcal{R}_1 - g_{rt}(\omega)}{\sqrt{\mathcal{R}_1}\left(1 - g_{rt}(\omega)\right)}. \tag{3.41}$$

The process of minimizing the fraction in Eq. 3.41 is called impedance matching.

We now determine a condition for impedance matching in the case of a bow-tie cavity. A bow tie cavity is made of four mirrors so $N = 4$, therefore the total reflectivity is:

$$\mathcal{R} = \mathcal{R}_1\mathcal{R}_2\mathcal{R}_3\mathcal{R}_4 =: \mathcal{R}_1\mathcal{R}_{234}, \tag{3.42}$$

where $\mathcal{R}_2$, $\mathcal{R}_3$, $\mathcal{R}_4$ are the reflectivity of the highly reflective mirrors while $\mathcal{R}_1$ is the reflectivity of the first mirror. The reflectivity $\mathcal{R}_1$ must be chosen to maximize the circulating power.
The other losses summarized by α in Eq. 3.39 are ideally only the loss from second harmonic conversion in the crystal. However, we must also take into account other losses such as the reflection at the anti-reflective (AR) coating for crystals cut at a right angle. Additionally further losses can occur through absorption in the crystal.
We discussed the possible losses in the cavity, and now consider the effect of second harmonic conversion in the crystal. The circulating power P'_{circ} after the crystal with non-linear coefficient κ_{NL} then is:

$$P'_{circ} = P_{circ} - \kappa_{NL}P_{circ}^2 \stackrel{!}{=} \alpha P_{circ}. \tag{3.43}$$

The resulting fraction of the circulating power from Eq. 3.39 consequently becomes:

$$\left.\frac{P_{circ}}{P_{inc}}\right|_{\omega=\omega_q} = \frac{1-\mathcal{R}_1}{\left(1 - \sqrt{\mathcal{R}_1\mathcal{R}_{234}\left(1-\kappa_{NL}P_{circ}\right)}\right)^2}. \tag{3.44}$$

This equation cannot be solved analytically for the circulating power P_{circ}. However, for the later calculations, numerical solutions are used in Sec. 5.3. Assuming the reflection power of all other mirrors $\mathcal{R}_{234}$ is set, it is possible to maximize the circulating power as a function of $\mathcal{R}_1$. This impedance matching is fulfilled if the reflected power vanishes. From Eq. 3.41, this corresponds to:

$$\mathcal{R}_1 - g_{rt}(\omega) \stackrel{!}{=} 0 \Rightarrow \mathcal{R}_1 = \mathcal{R}_{234}\cdot\alpha = \mathcal{R}_{234}\left(1-\kappa_{NL}P_{circ}\right). \tag{3.45}$$

Making use of Eq. 3.44, the formula for $\mathcal{R}_1$ becomes:

$$\begin{aligned}\mathcal{R}_1 &= \mathcal{R}_{234}\left(1 - \kappa_{NL}\frac{1-\mathcal{R}_1}{\left(1-\sqrt{\mathcal{R}_1\mathcal{R}_{234}\left(1-\kappa_{NL}P_{circ}\right)}\right)^2}P_{inc}\right)\\ &= \mathcal{R}_{234}\left(1 - \kappa_{NL}\frac{1-\mathcal{R}_1}{\left(1-\sqrt{\mathcal{R}_1\mathcal{R}_{234}\alpha}\right)^2}P_{inc}\right).\end{aligned} \tag{3.46}$$

Solving this equation for $\mathcal{R}_1$ leads to the impedance matching condition:

$$\mathcal{R}_1 = \frac{1}{2}\left(1 + \mathcal{R}_{234} - \sqrt{1 - 2\mathcal{R}_{234} + \mathcal{R}_{234}^2 + 4\mathcal{R}_{234}\kappa_{NL}P_{inc}}\right). \tag{3.47}$$

This condition gives the reflection power of the incoupling mirror for a maximized circulating power. For the design of the cavities, we know the values for κ_{NL}, $\mathcal{R}_{234}$ and P_{circ} and can simply calculate the optimum $\mathcal{R}_1$.
In this section we were able to formulate a stability condition for optical resonators using the matrix formulation of ray optics. Extending our discussion to Gaussian beams led us to a self-consistency condition for a Gaussian beam inside a resonator. Applying these conditions to the hemispherical and bow-tie cavity allowed us to describe the incoupling of the infrared laser into the ULE cavity and determine formulas for geometric parameters important to the design of the doubling cavities. Finally, we defined characteristic values for resonators in general and derived an impedance matching condition in the particular case of the bow-tie cavity.

4 Locking Methods

For most purposes commercial lasers require further frequency stabilization. This also applies to the infrared laser used in this work. In our case, frequency stabilized UV light is achieved by first applying stabilization to the source, the infrared laser. Additionally, the doubling cavities need to be stabilized in length, to enable the incoupling of light (see Sec. 3.4). Both these endeavors require stabilizing methods, which are explained in this Section. The underlying principle is to use the periodically occurring cavity resonances, for which the light field builds up in the resonator. For the frequency stabilization of the infrared laser we use the ULE cavity and we achieve length stabilization in the doubling cavity itself. These cavity resonances are Lorentzian peaks in the transmission signal as described in Sec. 3.4. Frequency and length stabilization can be achieved by building a feedback system which corrects for any deviation from the peak. The two locking methods relevant for this thesis are the Pound-Drever-Hall (PDH) and the Haensch-Couillaud (HC) locking methods. We use the first method for the frequency stabilization of the infrared laser and the length stabilization of the first doubling cavity. We use the second method for the length stabilization of the second doubling cavity.

4.1 Pound-Drever-Hall Lock

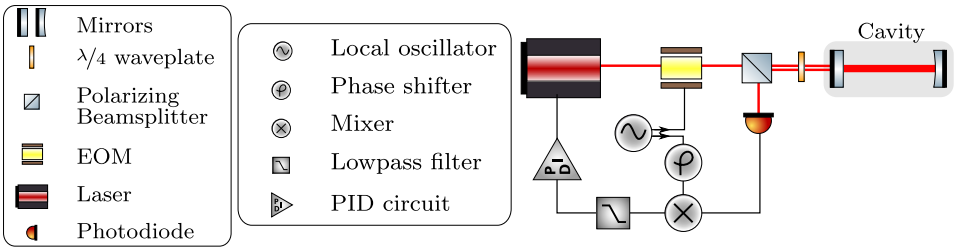

Figure 4.1: Schematic drawing of the necessary components for a Pound-Drever Hall lock

As we saw in Sec. 3.1, the light field only builds up if half the wavelength of the laser fits an integer number of times into the cavity length, or in other words the frequency is an integer number of the cavity's free spectral range $\Delta\nu_F$. The goal of locking techniques is then to keep the frequency of the laser close to these fixed frequencies of the cavity. In the case of a length stabilization, the cavity length is adjusted to stay on resonance instead of the frequency assumed fixed.

The PDH locking method uses the reflection signal of the light coming back from and out of the cavity. Close to resonance the reflected signal is almost zero. This method stabilizes the frequency or length by keeping the reflection signal at zero.

In the following we derive the formula for the error signal of the PDH locking method. The corresponding optical and electronic setup for this method is shown in Fig. 4.1. If the signal deviates from the minimum reflection signal, it is still unknown whether the frequency or length is too high or too low. At this stage we do not not know in which direction to correct for the deviation. However, if the signal is modulated, for example sinusoidally, the sign of the frequency derivative, is negative on the falling and positive on the rising edge. Therefore, the signal sent into the cavity is modulated with a frequency by using an electro-optical modulator (EOM) or by modulation of the laser current. In both cases the modulated light is of the form [48]:

$$\mathcal{E}_{inc} = \mathcal{E}_0 e^{i(\omega t + \beta \sin(\Omega t))}, \tag{4.1}$$

where ω is the frequency of the light, $\mathcal{E}_0$ its field amplitude, β the modulation strength and Ω the modulation frequency. Expanding this field in terms of Bessel functions for small β leads to:

$$\begin{aligned}\mathcal{E}_{inc} &\approx \mathcal{E}_0\left(J_0(\beta) + 2iJ_1(\beta)\sin(\Omega t)\right)e^{i\omega t} \\ &= \mathcal{E}_0\left(J_0(\beta)e^{i\omega t} + J_1(\beta)e^{i(\omega+\Omega)t} - J_1(\beta)e^{i(\omega-\Omega)t}\right),\end{aligned} \tag{4.2}$$

where J_i are the Bessel functions of order i. This approximation for a small modulation strength β shows that the incoming field is made up of three contributions with frequencies ω and $\omega \pm \Omega$ and weighed by the Bessel functions. The power of the initial beam $P_0 = |\mathcal{E}_0|^2$ is therefore composed of the carrier and two sideband powers $P_0 = P_c + 2P_s$, with $P_c = J_0^2(\beta)P_0$ the carrier power and $P_s = J_1^2(\beta)P_0$ the sideband power. With these expressions it is possible to calculate the reflected field:

$$\mathcal{E}_{ref} = \mathcal{E}_0\left(F(\omega)J_0(\beta)e^{i\omega t} + F(\omega+\Omega)J_1(\beta)e^{i(\omega+\beta)t} - F(\omega-\Omega)J_1(\beta)e^{i(\omega-\beta)t}\right), \tag{4.3}$$

where $F(\omega)$ is a function which takes into the account the accumulated phase ϕ during a roundtrip in the cavity and the finite reflectivity of the mirrors r in an otherwise loss-free resonator. It is of the form:

$$F(\omega) = \frac{\mathcal{E}_{refl}}{\mathcal{E}_{inc}} = \frac{r\left(e^{i\phi}-1\right)}{1-r^2e^{i\phi}} = \frac{r\left(e^{i\frac{\omega}{\Delta\nu_F}}-1\right)}{1-r^2e^{i\frac{\omega}{\Delta\nu_F}}}, \tag{4.4}$$

where the second part of the equation is written for the case of a varying frequency ω, with $\Delta\nu_F$ the free spectral range of the two mirror cavity. The quantity measured in experiments is the reflected power:

$$\begin{aligned}P_{ref} =& P_c|F(\omega)|^2 + P_s\left(|F(\omega+\Omega)|^2 + |F(\omega-\Omega)|^2\right) \\ &+ 2\sqrt{P_cP_s}\Re\left[F(\omega)F^*(\omega+\Omega) - F^*(\omega)F(\omega-\Omega)\right]\cos(\Omega t) \\ &+ 2\sqrt{P_cP_s}\Im\left[F(\omega)F^*(\omega+\Omega) - F^*(\omega)F(\omega-\Omega)\right]\sin(\Omega t) + (2\Omega \text{ terms}).\end{aligned} \tag{4.5}$$

It carries the relevant phase information of the carrier through the terms oscillating with Ω. In the limit of a high modulation frequency and close to a resonance $F(\omega \pm \Omega) \approx -1$. We can then write the coefficient in front of the oscillating terms in Eq. 4.5 as:

$$F(\omega)F^*(\omega+\Omega) - F^*(\omega)F(\omega-\Omega) \approx -2i\Im[F(\omega)]. \tag{4.6}$$

This expression is purely imaginary. Therefore the only term oscillating with Ω in Eq. 4.5 is the sine function. The process of extracting the coefficient in front of the sine function is called demodulation. It is achieved by multiplying the electric signal from the photodiode with another sine function. This function is generated by the same oscillator as the one used for the EOM and has a frequency Ω'. The product of these two sine functions of frequencies Ω and Ω' can also be written as:

$$\sin(\Omega t)\sin(\Omega' t) = \frac{1}{2}\left[\cos\left((\Omega-\Omega')t\right) - \cos\left((\Omega+\Omega')t\right)\right]. \tag{4.7}$$

By choosing the second frequency Ω' to be the same as Ω, the modulation frequency, the first term in Eq. 4.7 becomes a constant DC-term. However, if we choose to multiply with a cosine term, both contributions become sine functions, and by setting Ω and Ω' equal, the part which previously became a DC term is zero. However, changing a cosine function to a sine, is only a matter of introducing a phase shift of 90°. Therefore, it is necessary to be able to adjust the phase of the signal with which the photodiode signal is multiplied or to introduce a phase shifter in the setup. All in all, we multiply the reflected signal with a sine function, send it through a subsequent low-pass filter, and extract an error signal ε of the form:

$$\varepsilon = 2\sqrt{P_sP_c}\Im\left[F(\omega)F^*(\omega+\Omega) - F^*(\omega)F(\omega-\Omega)\right]. \tag{4.8}$$

An example of such an error signal can be found in Sec. 6.2 and 7.3. Close to resonance, we can use the approximation from Eq. 4.6 and obtain the following equation for $F(\omega)$:

$$F(\omega) \approx i\frac{r}{1-r^2}\phi \approx i\frac{\mathcal{F}}{\pi}\delta\phi. \tag{4.9}$$

The last approximation is made under the assumption of a high finesse $\mathcal{F}$. If the accumulated phase stems from changes in the cavity length l, and is close to resonance, it is of the form $\phi = 2\pi N + 4\pi\delta l/\lambda$. However, if the changes come from the frequency modulation the phase is $\phi = 2\pi N + \delta\omega/\Delta\nu_F = 2\pi N + 4\pi l\delta\nu/c$, with $N \in \mathbb{N}$. The resulting error signals for both cases are:

$$\varepsilon|_{\text{near resonance}} \approx -8\sqrt{P_c P_s}\frac{\mathcal{F}}{\lambda}\delta l \tag{4.10}$$

$$\varepsilon|_{\text{near resonance}} \approx -8\sqrt{P_c P_s}\frac{\mathcal{F}l}{c}\delta\nu. \tag{4.11}$$

It becomes clear that close to resonance, the error signal is linear in the scanned parameter, whether that is the cavity length or the frequency. This linearity is later used in Sec. 6.3 to assign a linewidth to the frequency stabilized infrared laser.

With Eq. 4.8 we now have an error signal, which is zero when the frequency or length is on resonance. It also changes sign when the frequency or length go over the resonance, making it possible to distinguish between a too high and too low values.

4.2 Haensch-Couillaud Lock

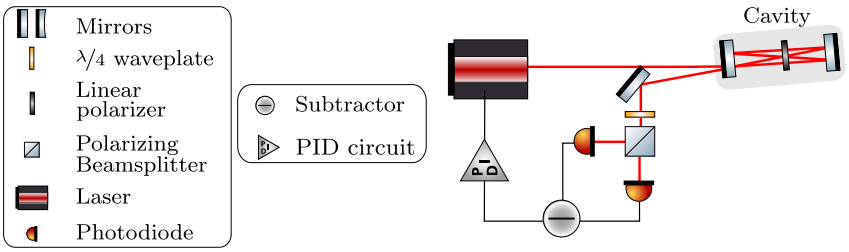

Figure 4.2: Schematic drawing of the necessary components for a Haensch-Couillaud lock

For the second doubling stage the sidebands typical for the PDH method become problematic for our application. As these sidebands are only partly filtered by the cavity, they could become resonant with a Rydberg transition and lead to a resonant Rydberg excitation. The Haensch-Couillaud locking method first proposed by Haensch and Couillaud in 1980 [49] does not require sidebands. However, it is necessary to have a polarizing element in the cavity, which is intrinsically given by a Brewster-cut crystal. In order to have an angle between the transmission axis of the crystal and the polarization of the light, we slightly tilt the polarization axis of the light away from its ideal position.

As demonstrated for the PDH method, we derive a formula and protocol to use this locking technique. The necessary optical components and electronics are shown in Fig. 4.2. We start by decomposing the linearly polarized light which is coupled into the cavity into a parallel and perpendicular part with respect to the polarizer's transmission axis:

$$\begin{aligned}\mathcal{E}_{\parallel}^{inc} &= \mathcal{E}_{inc}\cos(\theta)\\ \mathcal{E}_{\perp}^{inc} &= \mathcal{E}_{inc}\sin(\theta),\end{aligned} \tag{4.12}$$

where θ is the angle between the transmission axis of the polarizer and the polarization axis of the light, and $\mathcal{E}_{inc}$ the field amplitude of the incoming light. The amplitude of the reflected light analogously to the calculation in Sec. 3.4 can be written as:

$$\begin{aligned}\mathcal{E}_{\parallel}^{refl} &= \mathcal{E}_{\parallel}^{inc}\left(\sqrt{\mathcal{R}_1} - \frac{T_1}{\sqrt{\mathcal{R}_1}}\frac{\mathcal{R}e^{i\phi}}{1-\mathcal{R}e^{i\phi}}\right) \\ &= \mathcal{E}_{\parallel}^{inc}\left(\sqrt{\mathcal{R}_1} - \frac{T_1\mathcal{R}}{\sqrt{\mathcal{R}_1}}\frac{\cos(\phi)-\mathcal{R}+i\sin(\phi)}{(1-\mathcal{R})^2+4\mathcal{R}\sin^2\left(\frac{\phi}{2}\right)}\right),\end{aligned} \tag{4.13}$$

where $\mathcal{R}_1$ and T_1 are the reflection and transmission amplitude of the first mirror and $\mathcal{R}$ corresponds to the amplitude ratio after a whole roundtrip. The coefficient $\mathcal{R}$ takes into account losses from the mirrors as well as from the polarizer resulting in finesse of the form $\mathcal{F} = \pi\sqrt{\mathcal{R}}/1-\mathcal{R}$. The phase picked up during a roundtrip is accounted for by ϕ.
The perpendicular component is only affected by the first mirror:

$$\mathcal{E}_{\perp}^{refl} = \mathcal{E}_{\perp}^{inc}\mathcal{R}_1. \tag{4.14}$$

From the parallel field component in Eq. 4.13 and the perpendicular one in Eq. 4.14, it becomes apparent that on resonance $\phi = 2\pi n$ with $n \in \mathbb{N}$ both amplitudes are real and in phase. Therefore the field remains linearly polarized. However, the polarization is rotated from its initial position. On the other hand, for frequencies away from resonance the parallel component acquires a phase shift with respect to the perpendicular component. The result is an elliptical polarization which is the measured variable of this locking technique.

In the experimental setup, this phase shift is measured by sending the light through a $\lambda/4$ waveplate and subsequently a polarizing beamsplitter (PBS). The two outputs from the PBS are monitored by two photodiodes. The elliptically polarized light can be regarded the superposition of two counterpropagating linear components. The $\lambda/4$ waveplate then turns these components into linearly polarized waves which are separated by the subsequent PBS. If the light were linearly polarized, as is the case on resonance, both intensity outputs would be equal. In the case of an elliptical polarization, we assume the fast axis of the $\lambda/4$ waveplate to be along the polarization axis of the intra-cavity polarizer. With Jones calculus it is possible to write the field amplitudes after the waveplate and PBS as:

$$\mathcal{E}_{a,b} = \frac{1}{2}\begin{pmatrix}1 & \pm 1\\ \pm 1 & 1\end{pmatrix}\begin{pmatrix}1 & 0\\ 0 & i\end{pmatrix}\begin{pmatrix}\mathcal{E}_{\parallel}^{refl}\\ \mathcal{E}_{\perp}^{refl}\end{pmatrix}. \tag{4.15}$$

The resulting intensities measured by the photodiodes are:

$$I_{a,b} = \frac{1}{2}c\varepsilon\left|E_{a,b}\right|^2 = \frac{1}{2}c\varepsilon\left|\frac{1}{2}\left(\mathcal{E}_{\parallel}^{refl} \pm \mathcal{E}_{\perp}^{refl}\right)\right|. \tag{4.16}$$

The error signal is then obtained by subtraction of both intensities:

$$I_a - I_b = I^{inc}2\cos(\theta)\sin(\theta)\frac{T_1\mathcal{R}\sin(\phi)}{(1-\mathcal{R})^2 4\mathcal{R}\sin^2\left(\frac{\phi}{2}\right)} \tag{4.17}$$

with $I^{inc} = 1/2c\varepsilon\left|\mathcal{E}^{inc}\right|^2$ the intensity of the incoming beam. This error signal exhibits a steep slope on resonance and more slowly falling slopes outside of the resonance, yielding a wide capturing range.

In this section, we introduced the locking methods we later use for the frequency stabilization of the infrared laser and length stabilization of the two doubling cavities.

5 Results of the Parameter Optimization for the Doubling Cavities

In this Chapter we calculate the geometry and parameters necessary for building the doubling cavities. The basis for these calculations are the Boyd-Kleinman integral from Sec. 2.3, the stability and self-consistency conditions from Sec. 3.1 and 3.3 and the impedance matching from Sec. 3.4. We set the conditions in the cavities to yield maximum output power of the second harmonic light field, with the ultimate goal to have high power UV light.

This is required because we want to increase detuning to have longer lifetimes of the Rydberg dressed state. As higher detuning also leads to weaker interaction strength of the characteristic soft-core potential between Rydberg-dressed states, we need to compensate for this decrease. This can be achieved through a high Rabi frequency and therefore the optical power of the ultraviolet laser beam must be maximized.

We start by optimizing the Boyd-Kleinman factor for a maximum single-pass conversion. We then need to determine the geometric parameters of our cavities such that they fulfill the stability and self-consistency conditions. Finally, to increase the conversion further, we choose the mirrors of the cavity such that the impedance matching condition is fulfilled.

5.1 Boyd-Kleinman Integral

Optimizing the Boyd-Kleinman parameter is important to obtain high output powers of the second harmonic light. This is evident form the formula for the second harmonic power P_{out} from Sec. 2.3:

$$P_{out}(\sigma, B, \xi) = \frac{16\pi^2}{\varepsilon_0 c n_1 n_2 \lambda_1^3} \cdot d_{eff}^2 \cdot e^{-\alpha l} \cdot h\left(\sigma, B, \kappa, \xi, \mu\right) \cdot P_{in}^2 = \kappa_{NL} \cdot P_{in}^2, \tag{5.1}$$

with n_1, n_2 the refractive indices of air and the crystal respectively, d_{eff} the effective non-linearity of the crystal, $\alpha = {}^{(\alpha_1+\alpha_2)}/_2$ the mean of the damping coefficients of the fundamental and second harmonic, l the crystal length and $h\left(\sigma, B, \kappa\xi, \mu\right)$ the Boyd-Kleinman factor. The variable $\mu = {}^{(l-2f)}/_l$ describes the distance of the focus point from the middle of the crystal, which for symmetry reasons is set to zero. Also, κ which takes into account the absorption of the second harmonic beam in the medium is neglected, as the crystals are chosen to be transparent around this wavelength. The B-parameter accounts for the walkoff effect through $B = \rho\sqrt{l k_1}/2$ where ρ is the walkoff angle and is characteristic to a material and wavelength. Our goal is now to choose our tunable parameters such that Eq. 5.1 is optimized for high output power. These parameters are the phase mismatch parameter $\sigma = {}^{b\Delta k}/_2$ and the factor for focal strength $\xi = {}^l/_{2z_0}$. The Boyd-Kleinman integral then simplifies to [50]:

$$h\left(\sigma, B, \kappa = 0, \xi, \mu = 0\right) = \frac{1}{4\xi} \int_{-\xi}^{\xi} \int_{-\xi}^{\xi} d\tau\, d\tau' \frac{e^{-i\sigma(\tau-\tau') - \frac{B^2(\tau-\tau')^2}{\xi}}}{(1+i\tau')(1-i\tau)}. \tag{5.2}$$

For the optimization of the Boyd-Kleinman integral, we need material specific parameters and must therefore determine our non-linear crystals.

We choose Lithium Triborate (LBO) for the first doubling stage. The main advantage of LBO is its walkoff angle. It is smaller than usual values of other non-linear crystals by two orders of magnitude. This is a consequence of the non-critical phase matching, for which the beam propagation is along a crystal axis. This implies that the resulting beam profile is Gaussian (see Sec. 2.3) and the entire output power can be used. This is important for an efficient incoupling

of the light into the second doubling cavity. All LBO crystals are bought from Altechna and have the dimensions $3 \times 3 \times 20\,\mathrm{mm}^3$.

For the second doubling stage, the wavelength limits the crystal choice to either Beta Barium Borate (BBO) or Cesium Lithium Borate (CLBO). An advantage to CLBO, is that its walkoff angle is half as large as the one of BBO. Also, CLBO presents a higher damage threshold. The latter is advantageous as we will be working with high intensities. We therefore decided to use CLBO for the second cavity. However, CLBO is a hygroscopic material, which means that any exposure to air leads to absorption of water and to damages of the crystal structure. The crystal must therefore be continuously heated to about 405 K (corresponding to approximately 130 °C) and kept under vacuum [51]. Due to the extremely difficult handling of the CLBO crystals we also conducted all the calculations and designs for BBO as a backup crystal. The results are shown in Appendix A. The length of the CLBO and BBO crystals is kept smaller than for LBO to minimize the effect of walkoff. The overall dimensions of the CLBO and BBO crystals bought from Castech are $3 \times 3 \times 10\,\mathrm{mm}^3$.

The necessary crystal parameters for the optimization of the Boyd-Kleinman integral are taken from the SNLO database and are summarized in Tab. 3 [52].

Parameter	**Lithium Triborate (LBO)**	**Cesium Lithium Borate (CLBO)**	**Beta Barium Borate (BBO)**
Wavelengths $\lambda_1 \rightarrow \lambda_2$ [nm]	$1150 \rightarrow 575$	$575 \rightarrow 287.5$	$575 \rightarrow 287.5$
Refractive indices $n_\omega = n_{2\omega}$	1.603	1.495	1.67
Walk-off angle ρ [mrad]	3.9×10^{-1}	3.644×10^{1}	8.36×10^{1}
Effective non-linearity d_{eff} [pm/V]	8.41×10^{-1}	7.10×10^{-1}	1.84
Crystal length l [mm]	20	10	10
Temperature T [K]	334	405	355
Angle with optical axis θ [°]	90	54.3	42.9
Angle with second optical axis ϕ [°]	0	uniaxial crystal	uniaxial crystal

Table 3: Crystal parameters for the Boyd-Kleinman integral optimization from the SNLO program[52]

For the chosen crystals, we determine the maximum value for the Boyd-Kleinman integral, using the material parameters from Tab. 3. We calculate the real part of Eq. 5.2 for $\sigma \in [-3,3]$ and $\xi \in [0,5]$ and choose the σ and ξ with the highest h. In the cavity the parameter σ fixes the phase mismatch Δk through $\sigma = {}^{b\Delta k}/_{2}$ and ξ can be converted to the beam waist in the crystal w_c with $\xi = {}^{\lambda l}/_{2\pi n_2 w_c^2}$. The values of the integral for the LBO and CLBO crystals in this parameter range

are shown in Fig. 5.1a and 5.2a, respectively. The resulting values for a maximum h are:

$$\begin{aligned} h_{\mathrm{LBO}} &= 1.06 & h_{\mathrm{CLBO}} &= 0.0949 \\ \xi_{\mathrm{LBO}} &= 2.79 & \xi_{\mathrm{CLBO}} &= 1.46 \\ \sigma_{\mathrm{LBO}} &= -0.58 & \sigma_{\mathrm{CLBO}} &= -0.75. \end{aligned} \tag{5.3}$$

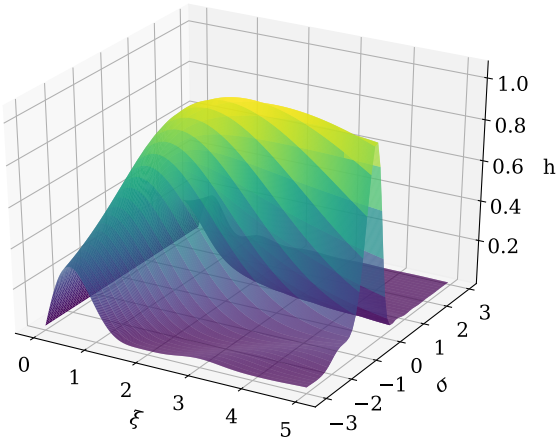

(a) Factor h as a function of ξ and σ

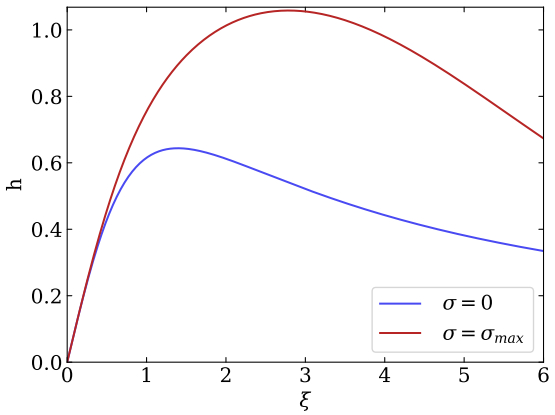

(b) Factor h as a function of ξ for $\sigma = 0$ and $\sigma_{max} = -0.58$

Figure 5.1: Boyd-Kleinman factor h for the LBO crystal with material parameters from Tab. 3

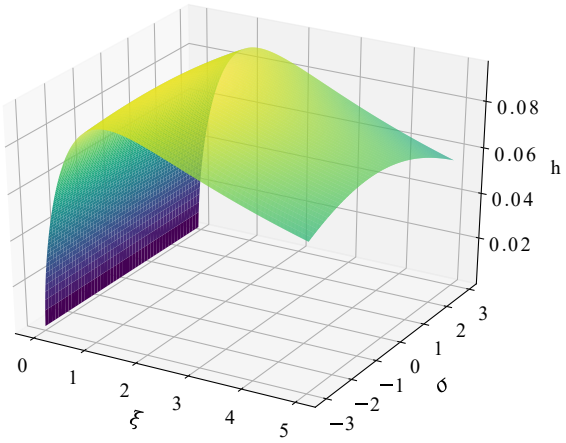

(a) Factor h as a function of ξ and σ

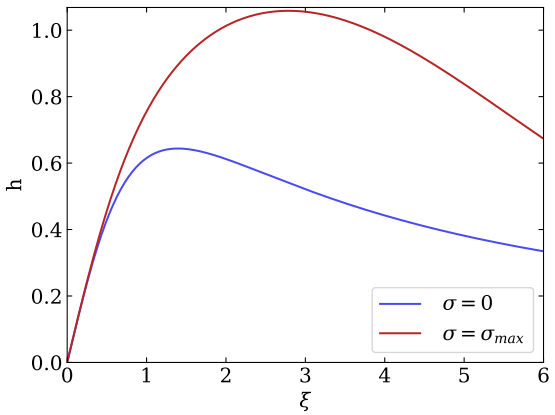

(b) Factor h as a function of ξ for $\sigma = 0$ and $\sigma_{max} = -0.75$: both curves lie almost exactly over each other

Figure 5.2: Boyd-Kleinman factor h for the CLBO crystal with material parameters from Tab. 3

It is apparent from Fig. 5.1a, that the value of h for LBO strongly depends on the phase mismatch parameter σ, which is not the case for CLBO, see Fig. 5.1a and 5.2a. We plotted h as a function of ξ for $\sigma = 0$ and for the maximum σ, and showed the results in Fig. 5.1b for LBO and in Fig. 5.2b for CLBO. For CLBO, we can set σ to zero for simplicity, because the resulting value for h only decreases by 2 %, the two curves almost exactly overlay in Fig. 5.2b. For LBO, we cannot make

this simplification without significantly decreasing the value of h, as apparent from Fig. 5.1b. Therefore we choose $\sigma = \sigma_{\mathrm{LBO}}$ which can be experimentally adjusted by tuning the temperature for a maximum output of the second harmonic power.

Another concern is the value ξ for highest h. Other sources [53], [54], [55], [56], [51] which have used LBO or CLBO for continuous-wave second harmonic generation move away from the Boyd Kleinman maximum and choose ξ smaller by a factor of two or three, which implies a larger waist inside the crystal. The reason for this choice is to stay below the damage threshold of the crystal and avoid thermal lensing from the high powers inside the crystal. For LBO and CLBO, we reduce ξ by a factor of three which decreases the Boyd-Kleinman factor by 20 to 30 %, see Fig. 5.1b and 5.2b. However, this decrease is only a reduction of the single-pass efficiency. It is therefore partly compensated by a higher circulating power. The final values for ξ, σ and the corresponding Boyd-Kleinman parameter for LBO and CLBO are:

$$\begin{array}{ll} h_{\mathrm{LBO}} = 0.72 & h_{\mathrm{CLBO}} = 0.074 \\ \xi_{\mathrm{LBO}} = 0.93 & \xi_{\mathrm{CLBO}} = 0.48 \\ \sigma_{\mathrm{LBO}} = -0.58 & \sigma_{\mathrm{CLBO}} = 0. \end{array} \tag{5.4}$$

This new choice of ξ shifts the value of the crystal waist from $w = 28.6\,\mu\mathrm{m}$ to $w = 49.6\,\mu\mathrm{m}$ for LBO and from $w = 20.5\,\mu\mathrm{m}$ to $w = 35.5\,\mu\mathrm{m}$ for CLBO.

We have determined the values for the beam waist by optimizing the single-pass output power. This now enables us to use them in the following section for the geometry optimization of the cavity.

5.2 Geometric Optimization

In the geometric optimization of the cavity we must account for the beam waist calculated in the preceding Section. To obtain this waist in the crystal, the lenses for the incoupling into the cavity must be chosen accordingly. However, to maintain and enhance the corresponding Gaussian mode inside the cavity, the self-consistency and stability conditions from Sec. 3.1 and 3.3 must be fulfilled.

The geometry of the cavity depends on how the crystal is cut. To reduce losses in the first doubling cavity, the LBO crystal we choose for this cavity can either be cut at a right angle and have an antireflective (AR) coating or be Brewster-cut. We favor the AR-coated LBO crystal for the following two reasons.

First, for the AR-coated LBO crystal, the beam of the second harmonic light presents a round profile. This is not the case for the Brewster-cut alternative, as the beam is projected onto a surface at an oblique angle and is therefore elliptic.

Second, the output efficiency of the cavity with an AR-coated LBO crystal is higher. To understand the reason for this higher efficiency we need to consider the losses generated by the crystals. For the AR-coated LBO crystal, these are the losses of the fundamental and second harmonic due to an imperfect antireflective coating. For the Brewster-cut LBO crystal, the second harmonic beam experiences losses as its polarization is perpendicular to the one of the fundamental beam from type I phase matching. These relatively high losses of the second-harmonic light are sufficient to lead to a lower efficiency than for the AR-coated LBO crystal.

However, there are conflicting reports on the sustainability of the AR-coating in the cavity because of the high circulating power. [50] reports on damages to the coating while [57] presents a functioning conversion, both with similar wavelengths and input powers. Therefore, to be able

to resort to the Brewster-cut crystal in case of damage to the coating, we optimize the geometry for both possibilities. We omit the calculations for the Brewster-cut LBO crystal in the following, but refer to Appendix A for more details.

For the second doubling cavity, there exists no AR coating which can withstand high circulating powers of green light and the high output power of the UV light. Therefore, we choose for the crystals in the second doubling cavity, the CLBO and BBO crystals, to be cut at a Brewster angle. Also, the ξ-parameter from the Boyd-Kleinman integral optimization and therefore waist for both crystals is almost identical and the Brewster angles only differ by 3°. Consequently, we can use the CLBO optimized geometry also for BBO.

In the following we optimize the geometry of the first doubling cavity for an AR coated LBO crystal and the second cavity for a Brewster-cut CLBO crystal. In a bow.tie cavity, we can optimize the following parameters: the curvature R of two of its mirrors, the length of the short and long arm d_s, d_l and the opening angle θ (see Fig. 3.21).

The mirror curvature is determined in retrospect: we start with a set of commonly used curvatures and calculate the corresponding short and long arm d_s, d_l and opening angle as later explained. We then check if these values can be translated to a cavity without any clipping of the beam or excessively large configurations and choose the value with the smallest geometry. We follow this procedure and obtain the following mirror curvatures for the first and second doubling cavity:

$$R_{\mathrm{LBO}} = 75\,\mathrm{mm} \qquad R_{\mathrm{CLBO}} = 50\,\mathrm{mm}. \tag{5.5}$$

With these radii of curvature, we can now calculate the length of the arms with the formula for self-consistency in a stable bow-tie resonator from Sec. 3.3 (Eq. 3.28). The resulting values are:

$$\begin{aligned} d_{s,\mathrm{LBO}} &= 75.8\,\mathrm{mm} & d_{s,\mathrm{CLBO}} &= 57.0\,\mathrm{mm} \\ d_{l,\mathrm{LBO}} &= 287.6\,\mathrm{mm} & d_{l,\mathrm{CLBO}} &= 141.3\,\mathrm{mm}. \end{aligned} \tag{5.6}$$

We must in the next step determine the opening angle θ. This angle introduces astigmatism which leads to the distinction between a sagittal and tangential plane. This distinction affects beam waists, curved mirrors and for CLBO additionally the Brewster-cut crystal. It is possible to calculate the waist w_c in the crystal and second waist w_2 in the long arm for the tangential and sagittal plane, as a function of the opening angle. For CLBO, there are two astimgatic optical elements, namely the Brewster-cut crystal and curved mirrors. For the right opening angle, they can compensate each other and lead to a round waist either in the crystal or in the second arm. To facilitate the incoupling into the cavity, the angle is chosen such that the second waist is round and the crystal waist is elliptical. For LBO, as there is no Brewster-cut interface, the angle is simply chosen to be as small as possible, to minimize the ellipticity of the second waist, but still large enough to make a reasonably sized cavity. The values for the second and crystal waist w_2, w_c in the sagittal and tangential plane as a function of the opening angle θ are plotted in Fig. 5.3 for LBO and in Fig. 5.4 for CLBO. The resulting angles are:

$$\theta_{\mathrm{LBO}} = 7.5° \qquad \theta_{\mathrm{CLBO}} = 14.3°. \tag{5.7}$$

In order to assess if the arm lengths from Eq. 5.6 are stable in both the sagittal and tangential plane, we determine the stability regions as a function of d_s and d_l for both planes separately. The resulting stability regions are shown in blue in Fig. 5.5 for LBO and Fig. 5.6 for CLBO. The offset between the self-consistency curve and stability regions is a result of the astigmatism taken into account for the calculation of the stability regions. Our chosen values for the arm lengths lie

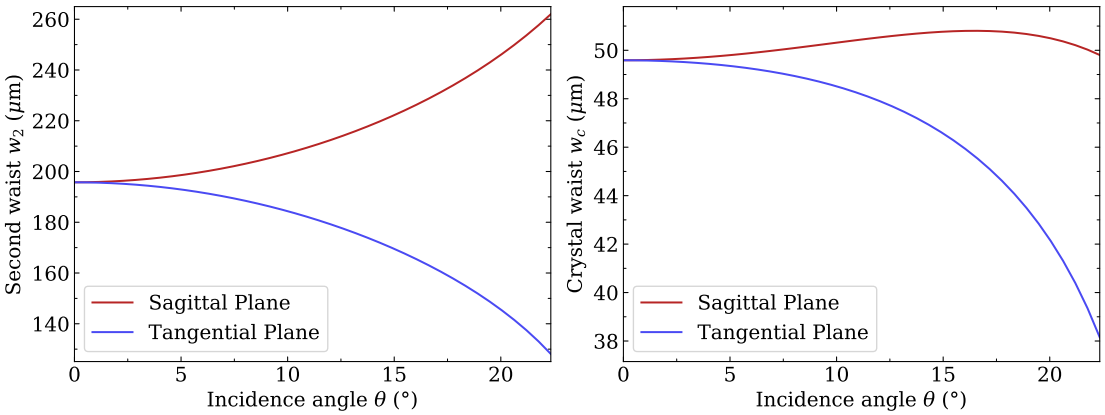

(a) Second waist in the long arm as a function of the incidence angle in the sagittal and tangential plane

(b) Crystal waist as a function of the incidence angle in the sagittal and tangential plane

Figure 5.3: Waist sizes as a function of the opening angle θ for the geometric considerations with the AR-coated LBO crystal

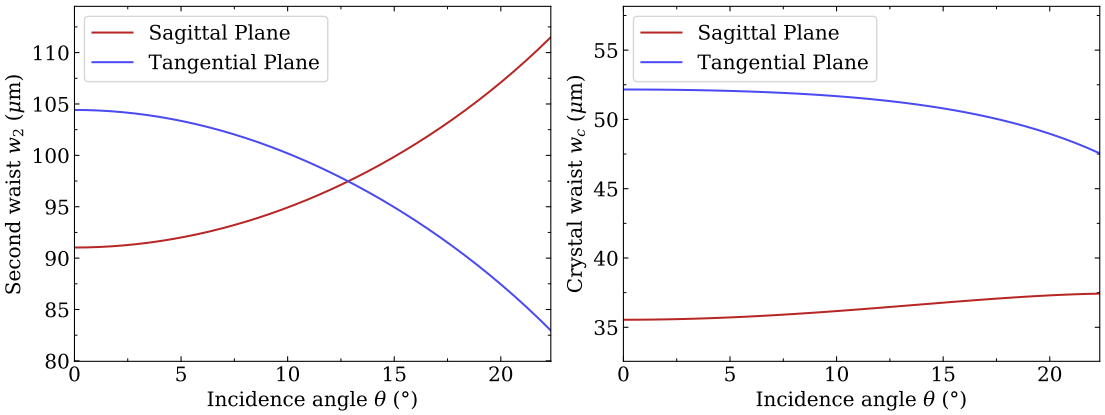

(a) Second waist in the long arm as a function of the incidence angle in the sagittal and tangential plane

(b) Crystal waist as a function of the incidence angle in the sagittal and tangential plane

Figure 5.4: Waist sizes as a function of the opening angle θ for the geometric considerations with the CLBO crystal

in the stable region for both the sagittal and tangential plane as indicated by blue markers in the Figures.

The self-consistency curves in the sagittal and tangential plane for LBO and CLBO have a slight offset relative to the stability regions. The curves are not entirely within the blue regions. The reason is the astigmatism taken into account for the calculation of the stability regions.

Tab. 4 summarizes the results which now determine the geometry of our cavities (see Sec. 7.1 for a drawing of the resulting cavity).

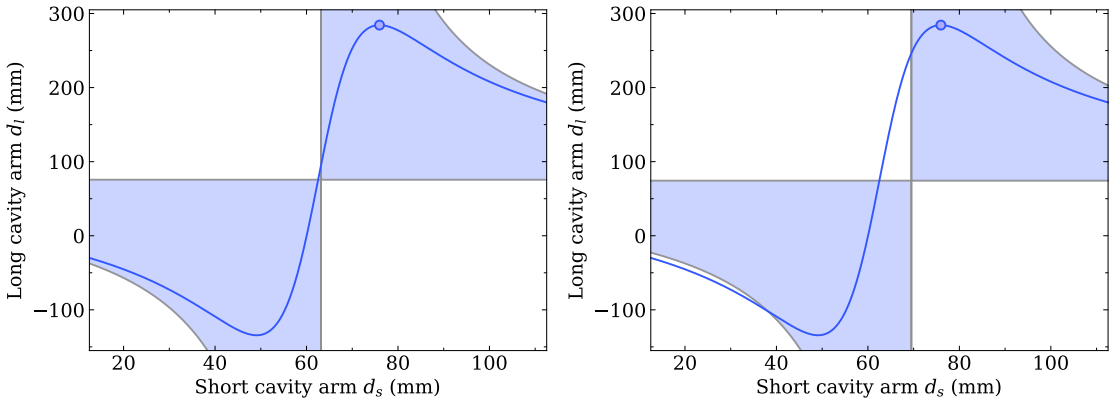

(a) Stability diagram in the sagittal plane as a function of the short and long arm d_s, d_l

(b) Stability diagram in the tangential plane as a function of the short and long arm d_s, d_l

Figure 5.5: Differing stability diagrams in the tangential and sagittal plane for the AR-coated LBO crystal: the blue regions indicate a stable resonator, the blue curve is a result of the self-consistency condition and the point indicates the choice of arm lengths in this thesis

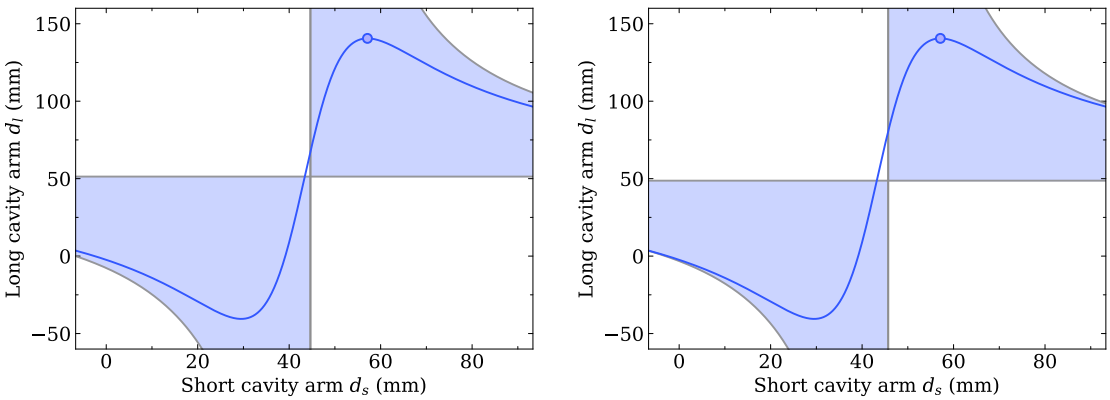

(a) Stability diagram in the sagittal plane as a function of the short and long arm d_s, d_l

(b) Stability diagram in the tangential plane as a function of the short and long arm d_s, d_l

Figure 5.6: Differing stability diagrams in the tangential and sagittal plane for the CLBO crystal: the blue regions indicate a stable resonator, the blue curve is a result of the self-consistency condition and the point indicates the choice of arm lengths in this thesis

Geometric parameter	AR-coated LBO)	Brewster-cut CLBO
Radius of curvature R	75 mm	50 mm
Short arm length d_s	75.8 mm	57.0 mm
Long arm length d_l	287.6 mm	141.3 mm
Opening angle θ	7.5°	14.3°

Table 4: Geometric parameters necessary for the construction of the cavity with the AR-coated LBO crystal and Brewster-cut CLBO crystal

5.3 Impedance Matching

Another component of the cavity which requires optimization is the reflectivity of the mirrors, as this affects the output power. Indeed, for maximum output power, the first mirror used for incoupling of the fundamental beam must fulfill the impedance matching condition from Sec. 3.4. This means that the reflected light at the incoupling mirror and the light exiting the cavity through that same mirror must interfere destructively. This is fulfilled for a specific reflectivity of the first mirror. The remaining three mirrors must be highly reflective for the incoming beam to keep roundtrip losses at the mirrors as small as possible, ideally much smaller than the losses generated by second harmonic conversion. Yet another requirement is that the fourth mirror must be AR coated for the second harmonic wavelength and therefore enable the outcoupling of the generated beam.

In the following we choose a reflectivity for the first mirror which ensures a partial impedance matching for a range of input powers. For LBO, we need a range of input powers because the maximal output power of the Raman Fiber Amplifier varies with wavelength. For CLBO, the second cavity's input is the output power of the first cavity. These values are only calculated but not confirmed experimentally, justifying the need for a range of input powers.

To increase flexibility, we want to be able to switch between different crystals and geometries in the two cavities. As the choice of crystals affects the reflectivity of our mirrors, we again optimize them for all options. The impedance matching calculation for the AR-coated LBO and BBO crystals can be found in Appendix A.

We use Eq. 3.44 to calculate the circulating power for varying input powers as a function of the first mirror's reflection coefficient. For this calculation the reflection of all the remaining mirrors must be known. This value is limited by what companies are able to produce for a reasonable price. The highly reflective mirrors used in this thesis were bought from Layertec and have a reflectivity of:

$$\mathcal{R}_{234,\mathrm{LBO}} = 0.9999^3 \qquad \mathcal{R}_{234,\mathrm{CLBO}} = 0.9995^3. \tag{5.8}$$

Other losses are reflections of the fundamental and second harmonic beam on the AR-coating of the LBO crystal. They are determined by the company which manufactured the crystal, in our case Altechna and are 0.25 % for the fundamental and 0.5 % for the second harmonic. For the Brewster-cut crystal, we have to take into account the losses from the refraction of the second harmonic light upon exiting the crystal, they are 14.6 %.

The circulating power also allows us to determine the output power P_{out} and conversion efficiency η:

$$\begin{aligned} P_{out} &= \kappa_{NL} \cdot P_{circ} \\ \eta &= \frac{P_{in}}{P_{out}}, \end{aligned} \tag{5.9}$$

where P_{in} is the input power of the fundamental beam. All three quantities are shown for LBO in Fig. 5.7 for input powers between 4 and 10 W. We only show the efficiency for CLBO in Fig. 5.8, for input powers between 1 and 7 W. The markers denote the maximum efficiency which can be achieved for a given input power.

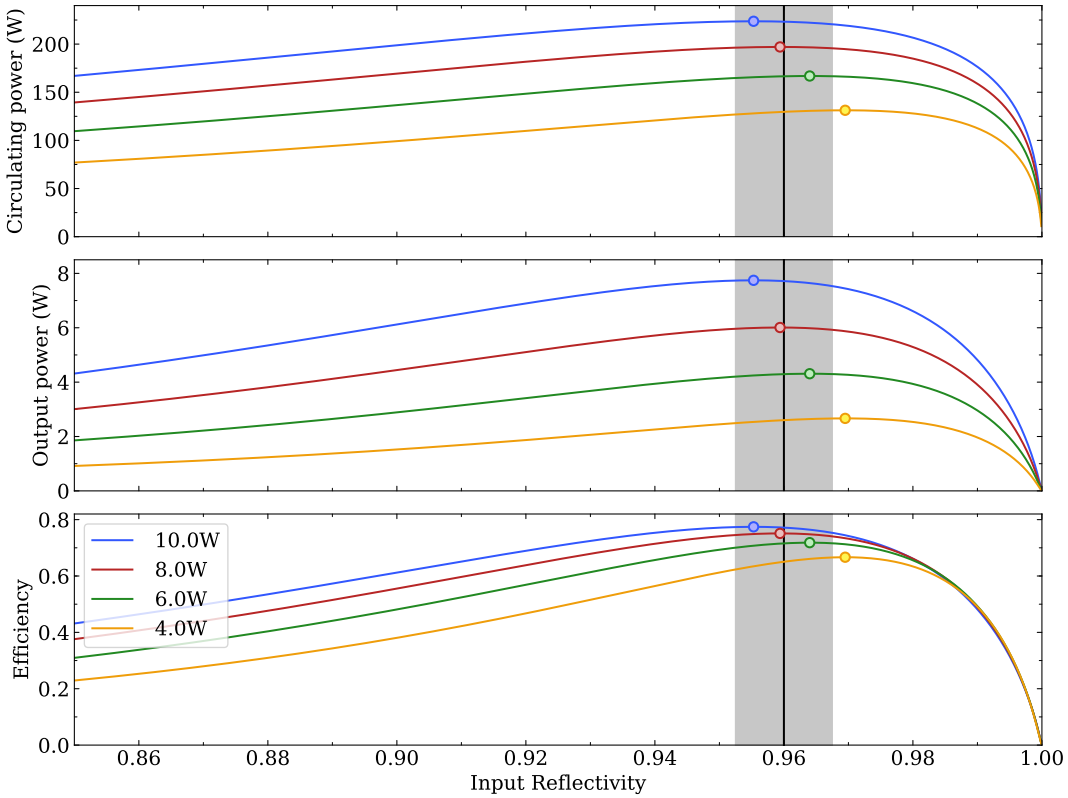

Figure 5.7: Circulating power, output power and efficiency for varying values of the reflectivity $\mathcal{R}_1$ of the first mirror for the AR-coated LBO crystal, realistic input powers lie between 8 and 10 W

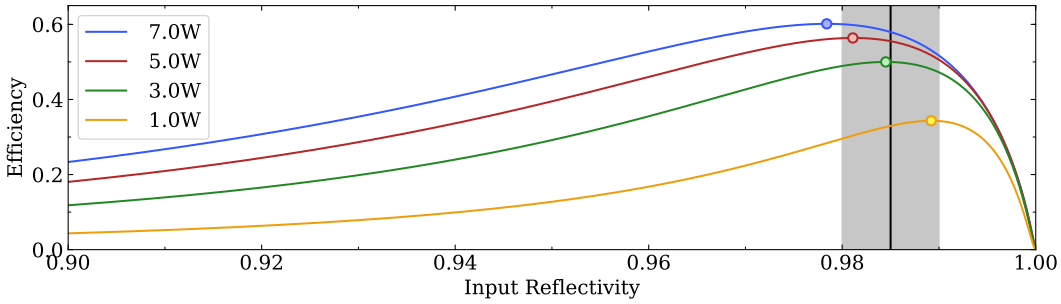

Figure 5.8: Efficiency for varying values of the input reflectivity $\mathcal{R}_1$ of the first mirror for the CLBO crystal, realistic input powers lie between 3 and 5 W

As can be seen from the Figures, the maximum efficiency decreases with increasing input power. Indeed, for high input powers the losses increase, due to increased second harmonic conversion. Hence the circulating power in relation to the input power is lower. Therefore the light leaking from the cavity through the first mirror has an amplitude which is lower relative to the incoming power. However, the light from the cavity and the one reflected at the first mirror must have equal amplitude to interfere destructively and this additional loss is compensated by lowering

the reflection of the first mirror. This means that the amplitude of the reflected light is lowered and the one of the leaked light increased.

Another important aspect of these curves, is the slowly increasing slope for reflectivities towards the maximum and a faster decrease to zero for reflectivities to the right of the maximum. In order not to be on the steep slope, we generally choose the reflection value to be smaller than the maximum value. The resulting values for the reflectivity are:

$$\mathcal{R}_{1,\mathrm{LBO}} = 0.96 \pm 0.0075 \qquad \mathcal{R}_{1,\mathrm{CLBO}} = 0.985 \pm 0.005 \tag{5.10}$$

The uncertainty of these values is given by the manufacturing companies and is depicted as grey areas in Fig. 5.7 and 5.8.

In this Chapter, we started with the Boyd-Kleinman integral to find an optimal waist inside the non-linear crystals of the doubling cavities. The geometric parameters of these cavities were then chosen to allow for this waist inside the crystal and fulfill the self-consistency and stability conditions. Finally, optimizing for a maximum circulating power through impedance matching led to a value for the reflectivity of the first mirror.

6 Infrared Laser System

In our setup, atoms are dressed with their Rydberg states using UV laser light. For Potassium the wavelength of the light must be tunable between 285.5 and 288.5 nm to access states from $N = 20$ to ionization. Therefore, the initial infrared laser source must be adjustable between 1142 and 1154 nm. Furthermore, the infrared light has to be frequency stabilized and power enhanced to reach a significant output power in the UV. We start by describing the optical setup built for the infrared laser system and the electronics necessary for the frequency stabilization of the laser. We then characterize the Pound-Drever-Hall lock onto a cavity made of Ultra Low Expansion (ULE) glass and conclude with the power enhancement through a Raman Fiber Amplifier (RFA).

6.1 Optical Setup and Electronics

We build an optical setup for the infrared laser system to serve the following functions: frequency stabilization, power enhancement and monitoring of the wavelength. A graphical overview of this setup and its most important components is shown in Fig. 6.1.

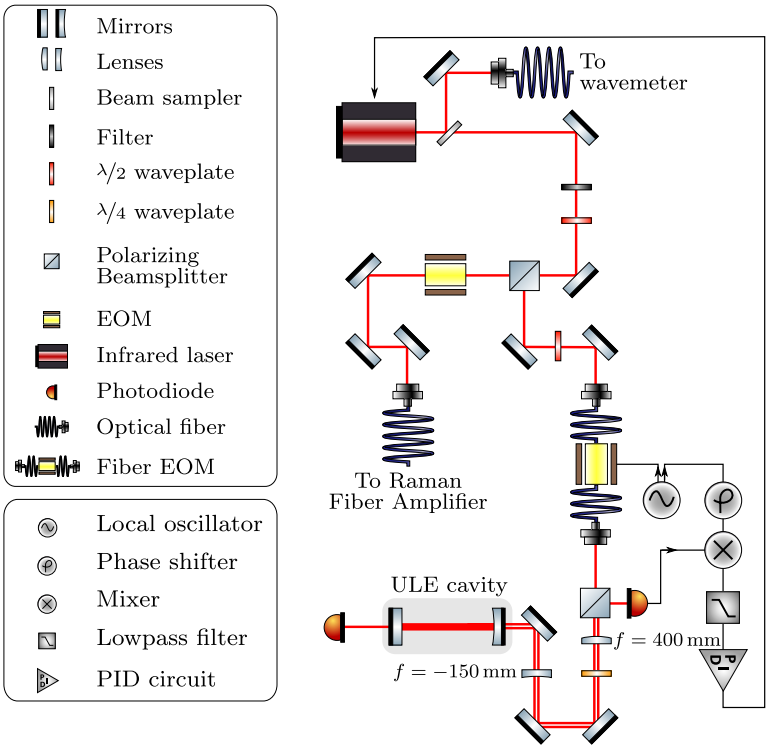

Figure 6.1: Optical setup for the infrared laser system, the detailed electronic setup for the PDH frequency stabilization of the laser is shown in Fig. 6.2

The infrared laser is a tunable external cavity diode laser from Sacher. It is built in a Littrow configuration: the wavelength-selective element in the laser cavity is a grating. The angle of this grating determines the output wavelength of the laser. It can be adjusted with a screw affixed to the laser housing. The accessible wavelength ranges from 1100.6 nm to 1188.3 nm, which includes the relevant wavelengths between 1142 and 1154 nm. The feedback loop for the frequency stabilization acts on the internal piezo of the laser which tunes the cavity length. A FET transistor allows for additional fast feedback by modulation of the current. It also has an internal

Faraday isolator to avoid any back-reflection into the laser, which could create an additional external cavity and lead to unstable operation of the laser. The output power for different operating currents at a wavelength of 1151 nm is shown in Fig. 6.5a. Throughout this thesis the laser is operated at 567.9 mA and kept temperature stabilized at 22.75 °C. The corresponding output power is 65.2 mW.

We now describe how the beam is divided and allocated to different functions as shown in Fig. 6.1. First, we separate a small portion of the beam with a beam sampler and couple a few µW into a multimode fiber attached to a wavemeter from Toptica, which monitors the wavelength of the light. We send the remaining beam through a $\lambda/2$-waveplate and a subsequent polarizing beamsplitter (PBS) to regulate the power of the two outputs of the PBS. After the beamsplitter, the part of the beam with most power is sent to the amplification stage in the Raman Fiber Amplifier (RFA). The RFA only amplifies light with a certain orientation of polarization. Therefore we need another $\lambda/2$-waveplate before the incoupling into the RFA to adjust the light's polarization. The other output of the PBS is sent into a fiber-coupled electro-optical modulator (EOM). This EOM has a high extinction ratio. Therefore, as for the RFA, we need one more $\lambda/2$-waveplate to adjust the polarization of the light.

We now address the setup needed for the frequency stabilization of the laser. The fiber-coupled EOM generates the sidebands for the PDH error signal as described in Sec. 4.1. After the EOM, the beam with about 100 µW is sent through a $\lambda/4$-waveplate and coupled into an Ultra-Low Expansion cavity, mode matched with two lenses. When the light frequency is off-resonance with the cavity, the beam is reflected back out of the cavity and sent trough the $\lambda/4$-waveplate again. The polarization is then perpendicular to the one coming out of the EOM and therefore deflected by the polarizing beam splitter. We then measure this reflection signal with a photodiode and use it for the generation of the PDH error signal. We also measure the transmission signal after the ULE cavity using a photodiode. It becomes non-zero on resonance. We scan the laser frequency to find the transmission peaks and reflection dips by applying a periodic ramp to its internal piezo which varies the laser cavity length and therefore its frequency.

We need to be able to choose arbitrary detuning for the Rydberg dressing, which means that we must be able to tune the laser frequency arbitrarily. However, this is problematic because the cavity's peaks onto which the laser frequency is locked are fixed by the ULE cavity's length. To circumvent locking onto the cavity's peaks, we generate additional peaks. Additionally to the frequency of the sidebands, we send another stable and tunable frequency signal to the EOM. This frequency can cover the whole spectral range of the ULE cavity. The laser frequency is then locked onto one of these new peaks which can be shifted in frequency and also have the necessary side peaks for the locking. The transmission signal with the resulting cavity peaks is shown in Fig. 6.4a. In this Figure the frequency for the sidebands is chosen to be $\nu_{PDH} = 21.7$ MHz and the one for the adjustable peaks $\nu_{large} = 340$ MHz. The smaller peaks are generated by the Rigol function generator. The frequencies for the adjustable peaks are generated by a direct digital synthesis device (DDS) which can produce frequencies up to 400 MHz. The ULE cavity's length is $l = 10$ cm and its free spectral range $\nu_{FSR} = c/2l = 1.5$ GHz. Therefore we need to double the DDS frequency to cover the entire range between cavity peaks. Both signals, from the function generator and the DDS are added and sent to the fiber-EOM.

The electronics necessary for the generation of new peaks and the sidebands are shown in Fig. 6.2.

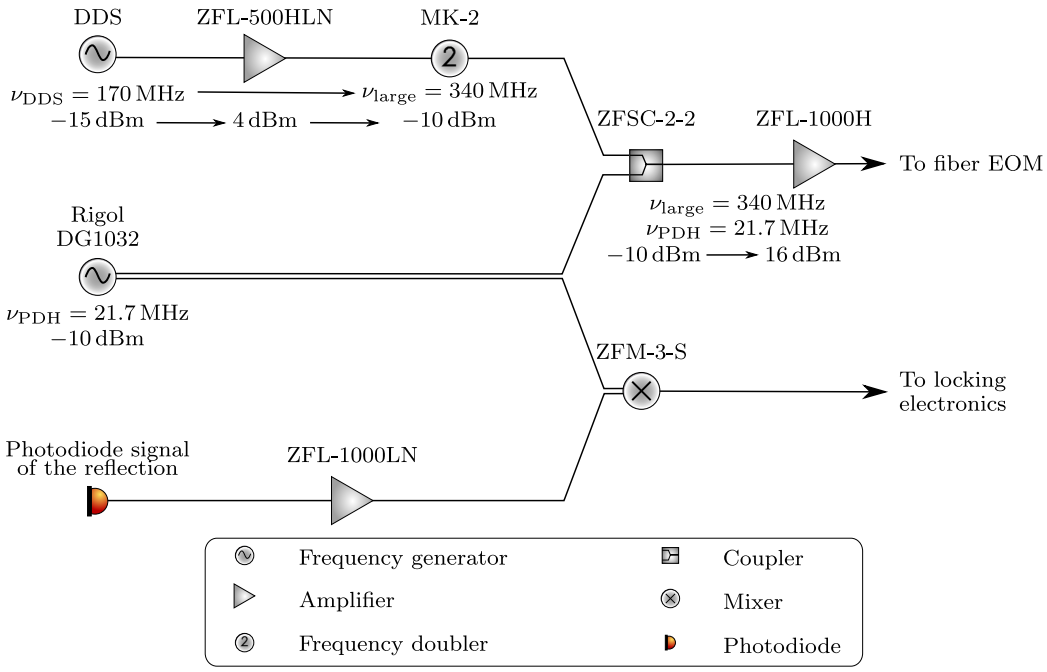

Figure 6.2: Electronic setup for the generation of peaks between the resonance peaks of the ULE cavity, all electronic components are from Mini-Circuits except for the function generators

6.2 Frequency Stabilization to an ULE Cavity

For the frequency stabilization of the infrared laser, we use a cavity made of Ultra Low Expansion glass from Advanced Thin Films. This synthetic material has a zero crossing of the expansion coefficient. The cavity's length is therefore very stable. It is a commonly used very precise reference, onto which the laser can be locked [58]. To reduce length fluctuations due to thermal drifts, the cavity's temperature is stabilized with Peltier elements and placed into two consecutive copper-shielding housings. The optical path length can also fluctuate due to changes of the refractive index of air, hence the cavity is placed under vacuum. A drawing of this system is shown in Fig. 6.3.

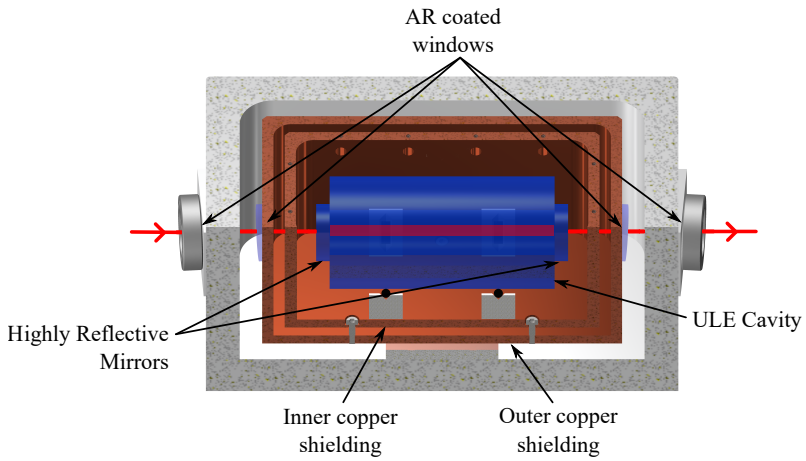

Figure 6.3: Cut through the ULE system placed under vacuum and two consecutive copper shieldings to avoid cavity length changes due to fluctuations of the refractive index of air or thermal drifts

For this ULE cavity, we need to find the cavity peak and generated peak at $\nu_{large} = 340\,\text{MHz}$. We choose a large scan range of the piezo within the laser, thus also increasing the scanned frequency range. To convert the x-axis from time to frequency, we use the small sidebands around the highest peak as reference. They are 21.7 MHz away from the main peak. Also we assume the axis to have a linear behavior in frequency and can therefore rescale it with the reference given by the distance to the sidebands. The transmission signal showing a cavity peak and a peak generated with the DDS frequency is displayed in Fig. 6.4a. To lock the laser, the scan range of the piezo is reduced until only the main cavity peak and its sidebands are visible on the transmission signal as seen in Fig. 6.4b. The corresponding PDH signal is shown in Fig. 6.4c. The feedback to the laser is converted into a current modulation for the fast deviations from resonance, and the piezo for slow drifts over time. We optimize the PID values of the feedback loop and show the resulting locked signal in Fig. 6.4e.

For the characterization of the laser's linewidth the frequency is locked onto one of the main peaks. As calculated in Sec. 4.1, close to resonance, the error signal is linear in the frequency. Therefore, a linear function is fitted to the measured error signal, yielding a slope of $a = -7.4 \times 10^{-7}\,\text{mV/Hz}$. Assuming the data points of the locked signal in Fig. 6.4e are in the linear range of the error signal, the unit of the y-axis can be converted to Hertz by diving the voltage value of each data point by the slope a. Every point x_i deviating from zero then corresponds to a deviation of the laser frequency with respect to the cavity peak and therefore the frequency onto which the laser is locked. To extract a linewidth from these deviations, we calculate the root mean square:

$$\text{RMS} = \sqrt{\frac{1}{N}\sum_{i=1}^{N}(x_i - \bar{x})^2}, \tag{6.1}$$

where N corresponds to the number of data points taken over 100 ms and $\bar{x}$ corresponds to the mean of the x_i. The resulting value is of approximately RMS = 80 kHz and shown as the grey delimitation in Fig. 6.4e. The linewidth is defined as the Full Width at Half Maximum (FWHM) and is therefore twice the value of the RMS:

$$\delta\nu = 160\,\text{kHz}. \tag{6.2}$$

With the optical electronic setup described in the previous Section we were able to frequency stabilize the infrared laser to a ULE cavity and obtained a linewidth of 160 kHz over 100 ms.

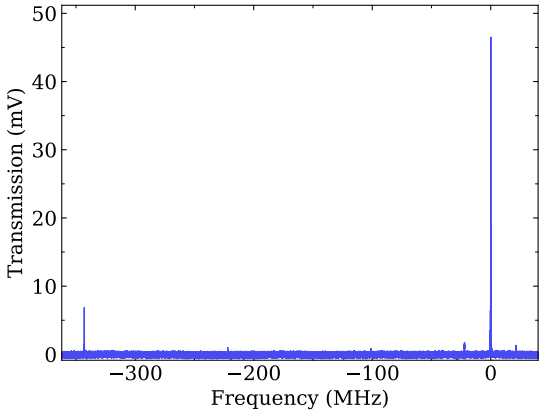

(a) Transmission signal showing the main cavity peak and the side peak as well as a TEM_{02} mode from imperfect incoupling

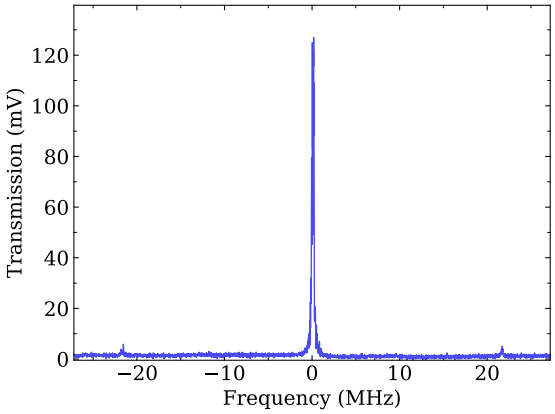

(b) Close-up of the main cavity peak with the generated side peaks at 21.7 MHz

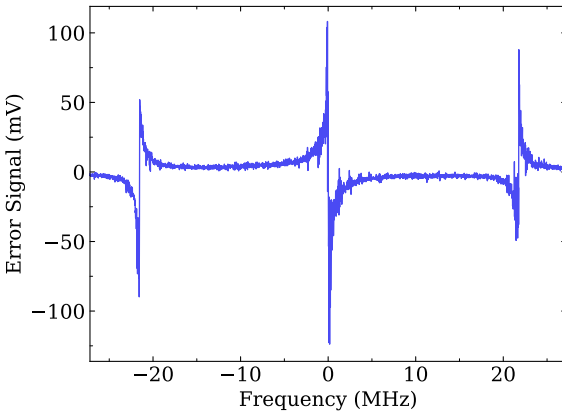

(c) PDH error signal corresponding to (b)

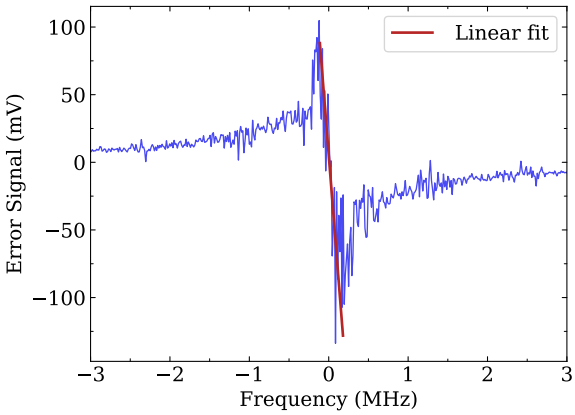

(d) Close-up of the error signal and the linear fit close to resonance with a slope $a = -7.4 \times 10^{-7}$ mV/Hz.

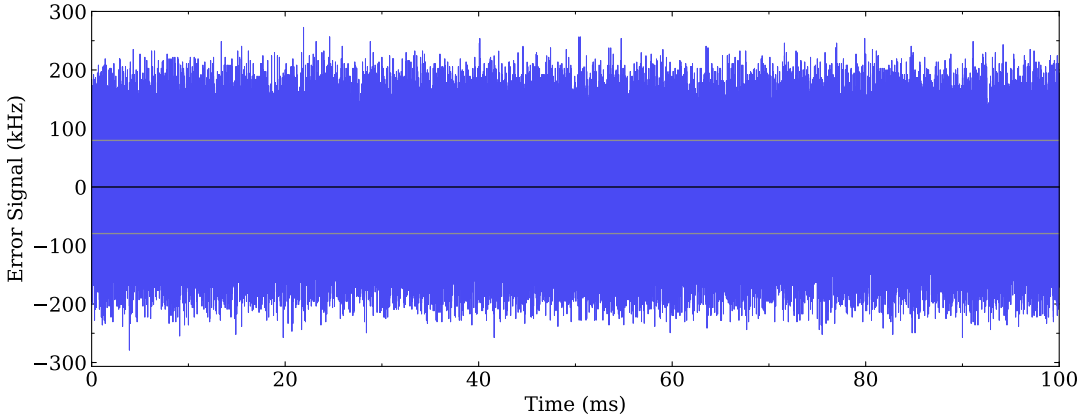

(e) Error signal with the feedback loop switched on: the grey line delimit the standard deviation of the signal

Figure 6.4: Measurements for the characterization of the frequency stabilizing lock of the infrared laser

6.3 Power Enhancement with a Raman Fiber Amplfier

Because we need high output powers in the UV, the amplification of the infrared laser system is important. In this part we characterize the power to current behavior of the laser itself and of the amplifying device, a Raman Fiber Amplifier from MPB Communications Inc.. The output power as a function of current at a wavelength of 1151 nm is shown in Fig. 6.5a for the laser and in Fig. 6.5b for the Raman Fiber Amplifier with a seed of 17 mW.

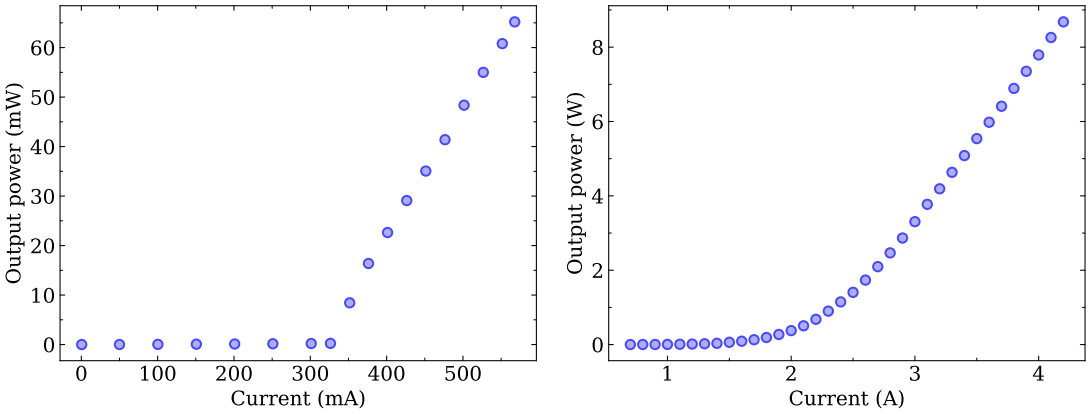

(a) Output power of the infrared laser as a function of current

(b) Output power of Raman Fiber Amplifier as a function of current with a seed of 17 mW

Figure 6.5: Characterization of the output power for the infrared laser and Raman Fiber Amplifier at a wavelength of 1151 nm

In this Section we have discussed the main elements of our infrared laser system. After having motivated the need to lock onto a tunable peak, we discuss the details of our locking procedure. We have also characterized the ensuing frequency stabilization of the laser with the PDH locking method. Finally, we have characterized the power behavior of both the laser and Raman Fiber Amplifier responsible for the power amplification. We successfully obtain high powers of up to 10 W.

7 First Doubling Cavity

The first second-harmonic-generation cavity is responsible for converting the infrared light tunable between 1142 and 1154 nm to green light of corresponding wavelengths between 571 and 577 nm. Its geometry and values for mirror reflectivity were optimized in Section 5. We now present the design of this cavity based on our theoretical calculations. We then characterize the performance of the cavity in operation, and determine its finesse by measuring the transmission signal. We show how the cavity length is locked with the Pound-Drever-Hall method and compare the resulting power of green light to calculations for the theoretically calculated cavity from Sec. 5. All measurements in this Section are obtained for a fundamental wavelength of 1143.8 nm, corresponding to $N \sim 60$.

7.1 Optical Setup and Cavity Design

We start by describing the optical setup surrounding the first doubling cavity which is depicted in Fig. 7.1. This setup is necessary for the coupling into the cavity and the Pound-Drever-Hall lock of the cavity length. All optical components and the doubling cavity itself are placed on a water-cooled breadboard to avoid any material expansion which could lead to misalignment.

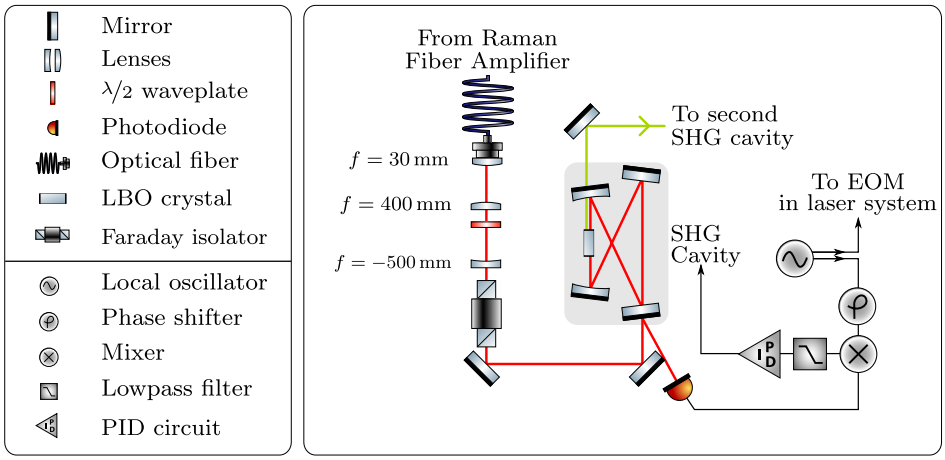

Figure 7.1: Schematic drawing of the optical setup surrounding the first doubling cavity

We start with the high-power output from the Raman Fiber Amplifier from the previous Section. We need to collimate the beam after the RFA. However, the optical fiber which provides the output light from the RFA has a Numerical Aperture (NA) smaller by a factor of 10 than commonly used optical fibers. It is therefore not possible to use the usual fiber outcouplers. Instead, we place a lens with focal length $f = 30$ mm at a distance f from the fiber output. To prevent dust from settling on the exposed fiber head, we cover the beam path between output and lense with tape partly made of anodized aluminum. Also, to keep any back-reflection of the cavity from traveling back into the RFA, we place a high power isolator from Toptica (SSR1150) in the beam path before the cavity. This isolator generates losses which are measured to be 10 %, which fits with the specifications from the manufacturer.

For the incoupling into the cavity, we use two lenses to obtain the second waist from Sec. 5.2, at the right position in the cavity. Also, the light must have the correct polarization with respect to the crystal inside the cavity. Thus we place an additional $\lambda/2$-waveplate in the beam before

coupling into the cavity.

The reflected light from the cavity has an angle with respect to the incoming beam, due to the non-zero angle of incidence. It is therefore possible to measure the reflection signal from the cavity directly. With this signal, we can assess the efficiency of the incoupling. Whilst scanning the cavity length, we examine by how much the reflection drops when the light is on resonance with a cavity peak. The reflection signal is also used to generate the Pound-Drever-Hall error signal. For the measurements in the following Sections the incoupling is measured to be approximately 65 %. The reasons for this value could be misalignment of mirrors or a wrong position of the lenses which would lead to a wrong value or location of the second waist.

We also measure the transmitted light, i.e. the green light exiting the cavity. Using the height of the transmission peak, we optimize the incoupling, the orientation of the cavity mirrors and the position of the crystal for a maximum output power.

In the following we describe the design of the cavity and its components. The cavity is made of an aluminum box which encloses a removable breadboard. Onto this breadboard, we place the cavity mirrors and the translational stage with the crystal holder. To showcase the cavity design, Fig. 7.2 presents the drawings for the second doubling stage. It only differs from the first doubling cavity by the specific values of the beam path geometry and the Brewster-cut crystal. For this qualitative discussion of the design and the components, the differences are insignificant.

The cavity housing made of aluminum is planned such that it can be evacuated, see Fig. 7.2a. The holes in the back of the cavity are for the access to the adjustment screws of the crystal's translational stage, a feedthrough for a connection to a vacuum pump, and electrical feedthroughs for the connection to the piezos, the heating elements and thermistor. The holes meant for the access to the translational stage, can be shut by using M10 screws and sealing rings. For the vacuum connection, we use KF – 16 connections and for the evacuation, a diaphragm pump. The electrical feedthroughs are achieved by using vacuum tight connectors provided by LEMO (HGP.0S.304CLLDV for the jacks and FLM.0S304.CLAD4 for the plugs). Inside the cavity we use capton-insulated wire which is designed for high vacuum. Other points of entry which must be vacuum tight are where the fundamental beam enters the cavity and the second harmonic exits it. For these points we use AR-coated windows made vacuum-tight by pressing the window with a sealing ring to the cavity with a metal mask.

The internal breadboard of the cavity (Fig. 7.2b) is also made of aluminum. It is fixed to the housing by using magnetic seats from Thorlabs (KBS98). The breadboard and housing are chosen to be two distinctive parts to avoid misalignment from the contraction of the latter when it is evacuated. To facilitate the alignment of the cavity we drill holes into the breadboard at the position of the mirrors, which we calculated in Sec. 5.2. To hold the mirrors, we use Polaris mounts from Thorlabs for half inch mirrors. To change the cavity length, we use two piezos from Piezomechanik, a small one (HPCH150/6-2/2) responsible for fast deviations from resonance and a larger one (HP St150/14-10/12) for slow drifts from resonance. The latter is also used to scan the cavity length to find the resonances, see Sec. 7.3. To achieve high bandwidths of the small piezo, it is glued onto a copper holder filled with soldering tin. This dampens the mechanical vibrations and pushes the resonance frequency to higher values [59]. Also the mirror glued onto the small piezo is a quarter inch mirror instead of half inch like the others and is only 2 mm thick, to avoid slowing it down due to the weight. The mirrors are glued onto both piezos by using the two-component glue Torrseal, intended for low-pressure environments.

Finally, we address the crystal holder shown in Fig. 7.2c. It must keep the crystal temperature stabilized and allow for translations in all directions and angles to optimize the alignment of the crystal with respect to the beam. We use a translational stage from Newport (9081-M) onto

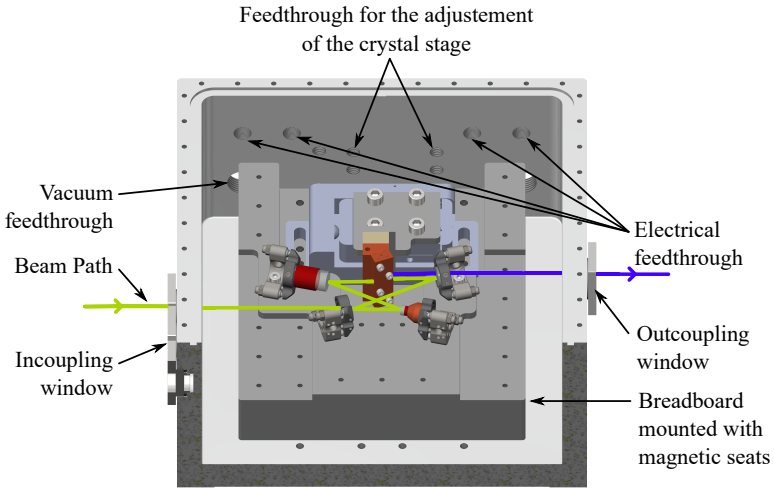

(a) Complete cavity drawing with the breadboard and crystal holder inside

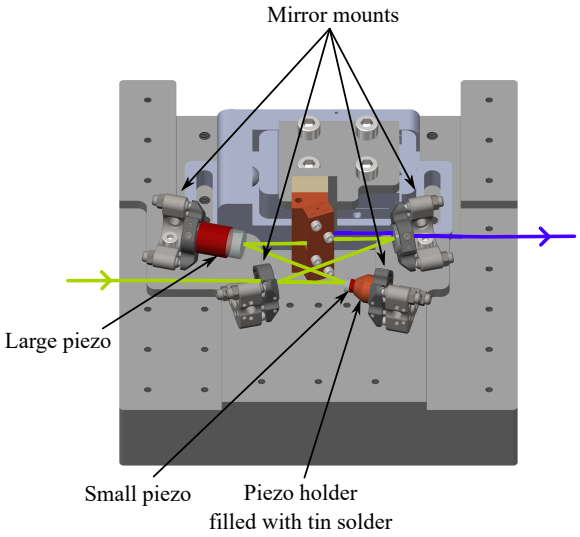

(b) Cavity breadboard with crystal holder and mirror holders at fixed positions

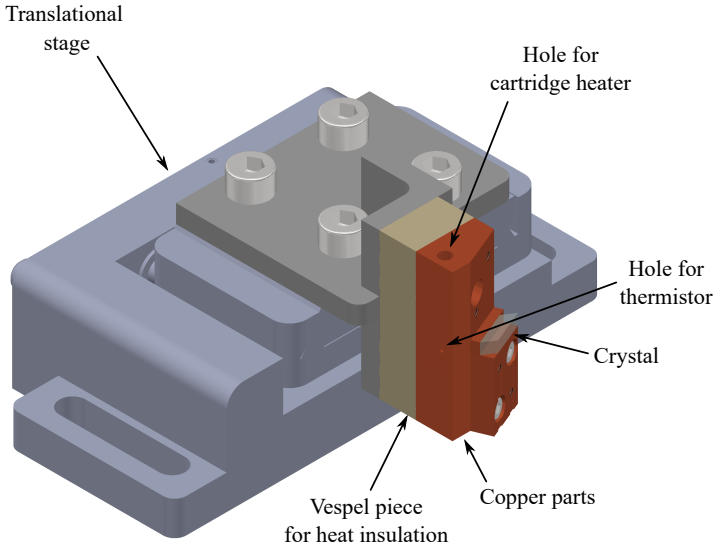

(c) Crystal holder for a Brewster-cut crystal: some of the copper parts are hidden for a direct view on the crystal

Figure 7.2: Drawing of the cavity with and without the housing and the crystal holder for the case of a Brewster-cut crystal

which we fix the actual crystal holder by using an intermediate piece made of stainless steel. The screws used to connect the stage and steel part are vented screws to avoid any pressure build-up from trapped volumes of air. To thermally decouple the heated crystal from the cavity we screw an intermediate block of Vespel inbetween the stainless steel and copper parts holding the crystal. Vespel is a material with low heat conductivity. Finally, the parts holding the crystal which are made of copper are screwed onto the Vespel. We drill holes into these parts to place a NTC thermistor from OMEGA and a resistive heating cartridge from Thorlabs (HT15W) close to the crystal. To assure good thermal contact of the thermistor and the heating element to the copper, we fill Indium foil into any space left in the hole of the heating element and fill thermally conductive and low outgasing epoxy (EPOTEC H74) into the hole for the thermistor. We use a Thorlabs controller (TC200) to monitor and regulate the temperature of the crystal. The crystals are sensitive to any mechanical stress applied to them and can break easily. Therefore we choose the dimensions of the copper parts such that there is enough space between copper and crystal to insert a layer of Indium foil. This assures both a softer contact surface compared to copper and a good heat conductivity. Three different kinds of crystal holders were designed to allow for the different cavity designs with the AR-coated and Brewster cut LBO crystals with dimension $3\times3\times20\,\mathrm{mm}^3$ and the CLBO and BBO crystals with both $3\times3\times10\,\mathrm{mm}^3$. For the Brewster-cut versions, the copper parts are such that the crystal is already in the beam path with the proper angle.

In this part we have described the optical setup built around the first doubling cavity. Also we have seen the design and purpose of the cavity and its components in detail.

7.2 Finesse and Free Spectral Range

In this Section we characterize the operating cavity by calculating the finesse for different input powers of the fundamental light. The expected values for the finesse can be calculated with the following formula:

$$\begin{aligned}\mathcal{F} &= \frac{\pi\sqrt{\left|g_{rt}(\omega)\right|}}{1-\left|g_{rt}(\omega)\right|} \\ &= \frac{\pi\left(\mathcal{R}_1\mathcal{R}_{234}\left(1-\kappa_{NL}P_{circ}\right)\right)^{1/4}}{1-\left(\mathcal{R}_1\mathcal{R}_{234}\left(1-\kappa_{NL}P_{circ}\right)\right)^{1/2}},\end{aligned} \tag{7.1}$$

where $g_{rt}(\omega)$ is the roundtrip function as defined in Sec. 3.3. The values for the reflectivity of the mirrors $\mathcal{R}_1$ and $\mathcal{R}_{234}$, the non-linear coefficient κ_{NL} and the circulating power P_{circ} are all taken from Sec. 5. The resulting values for $\mathcal{F}$ as a function of the input power are shown in Fig. 7.3c.

To determine the finesse in the experiment, we measure the transmission signal and error signal from the cavity at input powers of 2, 5 and 8 W. They are shown in Fig. 7.3a and 7.3b. The amplitude of the sidebands is too small to be seen on the transmission signal, therefore we use the error signal to rescale the x-axis to frequency values. The sidebands are 60 MHz away from the main peak. We then measure the frequency difference between two main cavity peaks, which defines the free spectral range $\Delta\nu_{FSR}$ and divide it by the peak width $\delta\nu$. We repeat this procedure for the three values of the input power. The resulting values for the finesse are shown as markers in Fig. 7.3c, where we have taken into account the coupling efficiency of 65 % and the isolator losses of 10 %. As we can see from this Figure, the calculated and measured values for the finesse differ by up to 40 %. A possible reason for this discrepancy is the measurement method. The value for the peak width is particularly sensitive to length fluctuations of the cavity during the scanning. However, the calculated and measured values are still of the same order of magni-

tude which is an acceptable result and indicates that our cavity parameters calculated in Sec. 5 yield a functioning doubling stage.

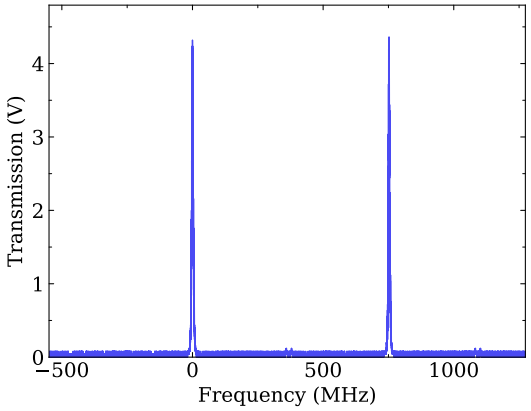

(a) Transmission signal showing two cavity peaks, with a full spectral range ν_{FSR} = 750 MHz. The sidebands next to the cavity peaks are not visible but we can see smaller peaks from higher cavity modes between the higher cavity peaks

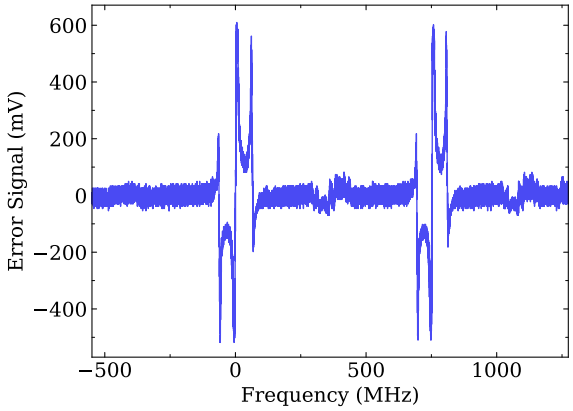

(b) PDH error signal corresponding to (a) and used to rescale the x-axis from time to frequency values. As in (a) we can see the higher modes through the small error signals in the middle of the spectrum.

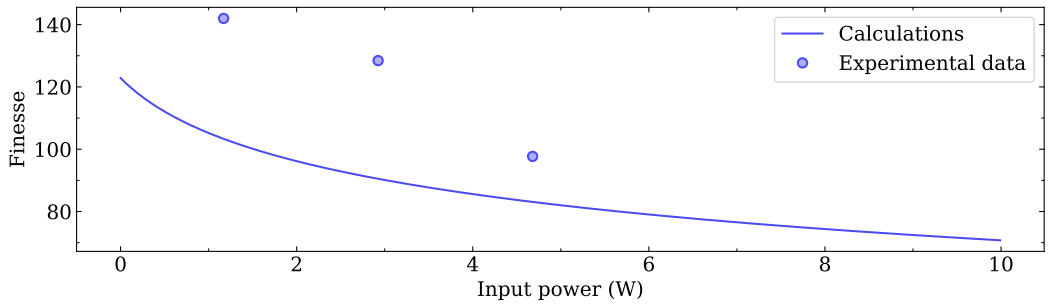

(c) Calculated and measured value for the finesse plotted respectively as the blue curve and points, we have taken into account isolator losses of 10 % and an incoupling efficiency of 65 %

Figure 7.3: Measurements of transmission and error signal at 5 W input power and comparison of the resulting finesse values for all input powers with calculations

7.3 Pound-Drever-Hall Lock

To maintain a high output power, the cavity length has to be locked onto the resonance. This is done by a Pound-Drever-Hall locking scheme (see Sec. 4.1). The sidebands are generated by an EOM before the Raman Fiber Amplifier (see Fig. 6.1) and are set to a frequency of 60 MHz. The feedback loop acts on the two piezos described in Sec. 7.1. The reflection signal and error signal are measured at an input power of 8 W, where losses from the isolator and incoupling are not taken into account. The measured PDH signal in the unlocked and locked state is shown in Fig. 7.4a and 7.4b respectively.

Similarly to the frequency stabilization lock of the infrared laser in Sec. 6.2, it is possible to calculate the Root Mean Square of the locked error signal to quantify the deviations from the resonance. However, expressing them in frequency is not applicable, as we deal with length stabilization. The resulting RMS is 0.03 mV and depicted by grey lines in Fig. 7.4b.

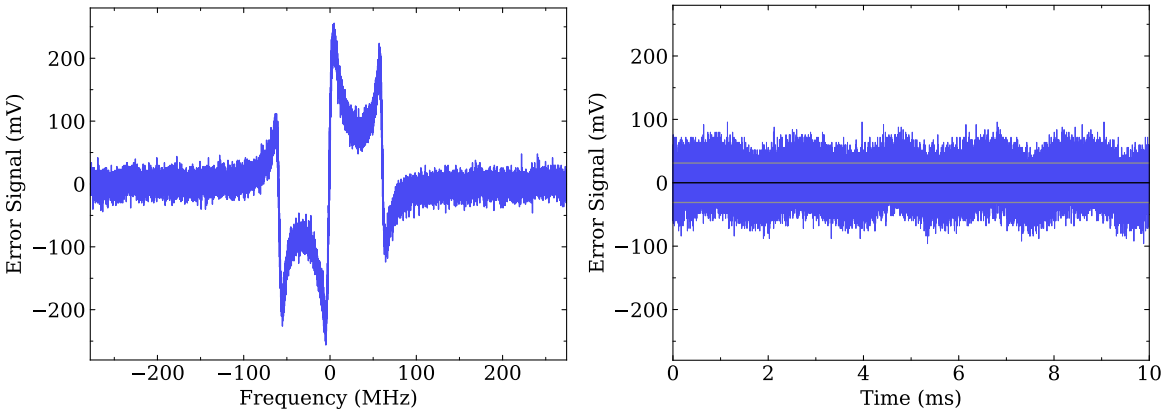

(a) Error signal of a cavity peak

(b) Error signal obtained when the feedback loop to the cavity is switched on and the PID values are optimized

Figure 7.4: Measurements for the length stabilization of the cavity by the Pound-Drever-Hall method

We have shown how the length of the cavity is stabilized to remain at maximum output by using the Pound-Drever-Hall locking technique.

7.4 Outgoing Power and Comparison to Simulations

In this Section we are interested in characterizing the output power of the second harmonic light. We compare the output power values we obtain in a length stabilized state of the cavity to calculations. To determine the output power with the cavity parameters from Sec. 5, we use the Eq. 3.44 and vary the input power instead of the reflectivity of the first mirror. The resulting values are shown in Fig. 7.5 as the blue curve.

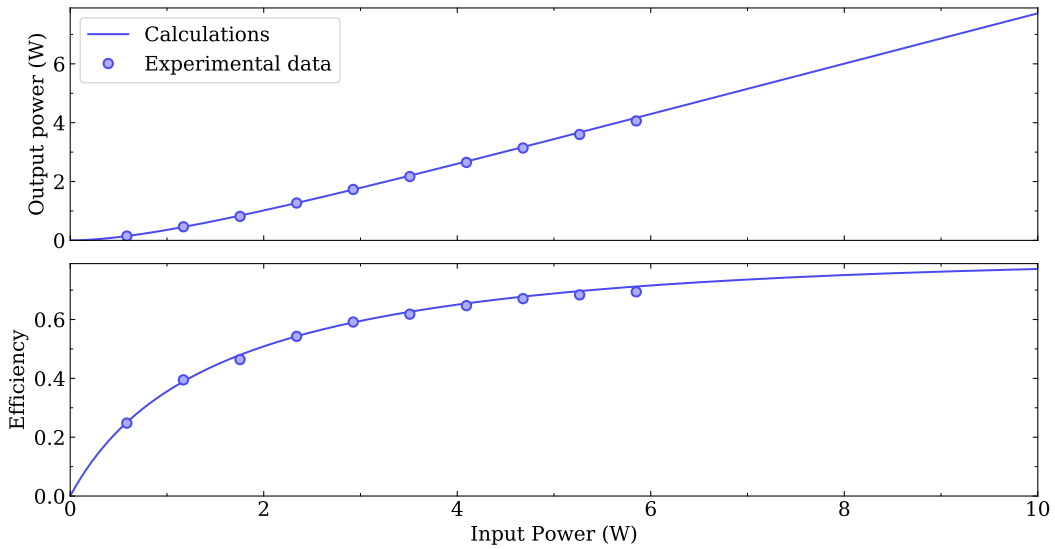

Figure 7.5: Plot of the theoretically calculated output power and efficiency and the actual measured values with the correction from the incoupling of 65 % and the isolator losses of 10 %

We measure values of the output power for input powers between 2 and 8 W in steps of 1 W.

For the data points in Fig. 7.5, we take into account the 10 % losses from the isolator and the coupling efficiency of 65 %. We can see that the calculated and measured values are in very good agreement. It is possible to obtain even higher output powers by further optimizing incoupling and alignment in the cavity.

In this Section, we have described the optical setup around the first doubling cavity and its design. We have characterized the cavity by measuring its finesse and output power and compared the values to our theoretical calculations. These comparisons prove that we have an operational cavity with the anticipated performance.

Conclusion

In this thesis we presented the design, construction and initial characterization of a setup for a one-photon transition in Potassium to Rydberg states. In particular, we designed two frequency doubling stages to transform light from an infrared laser to the UV light necessary for the transition. We discussed the performance of the infrared laser system and characterized the performance of the implemented first doubling cavity.

We have first discussed Rydberg atoms and in particular the possibility to use Rydberg dressing as a way to engineer long-range interactions between ultracold atoms. Long lifetimes and strong interaction of Rydberg-dressed states require a high-power laser source. For Potassium, this laser source must have a wavelength between 285.5 and 288.5 nm. This is best achieved with a laser system involving three steps: an infrared high power laser source, and two consecutive frequency doubling cavities.

To explain frequency doubling, we started by discussing the fundamentals of non-linear optical effects, in particular second harmonic generation. This led us to a formula for the second harmonic conversion of Gaussian beams. As nonlinear media we used an LBO crystal for the first doubling stage and a CLBO crystal for the second. With this formula and the parameters of the crystals we then optimized our setup to a maximum single-pass conversion efficiency for each doubling stage.

We placed the crystals in bow-tie cavities to increase the second harmonic power. Such cavities must fulfill two conditions: a stability condition and a self-consistency condition for a Gaussian cavity mode. On the basis of these conditions and taking into account the results from the single-pass conversion efficiency we calculated a geometry of the doubling cavities. The reflectivity of the cavities' first mirrors was determined by an impedance matching condition. This ensures maximum circulating power and yields higher second harmonic output power.

For the experimental setup we used an infrared laser and applied frequency stabilization with the Pound-Drever-Hall method. We achieved a linewidth of approximately 180 kHz and then increased the laser's output power using a Raman Fiber Amplifier to at least 8 W.

We then developed the design further and described the components of the first doubling cavity. Subsequently, we built the cavity based on the calculated and described design. We measured the output power of the cavity and obtained values of up to 4 W. We found that the cavity's performance exactly corresponds to the anticipated values. However, the position of mirrors and lenses could be further improved to avoid incoupling losses.

This work contribute to a setup which will use Rydberg dressed Potassium atoms to study many-body systems. To complete the setup from this work, the last remaining step is to build the second cavity and characterize its performance. With this final setup, we can proceed to actual experiments with Potassium.

Appendix

A Paramter Optimization for Alternative Second Harmonic Cavities

This Appendix shows the complementary calculations for the parameter optimization in Sec. 5.

We show the optimization of the Boyd-Kleinman integral from Eq. 5.1 for a BBO crystal of dimensions $3 \times 3 \times 10\,\mathrm{mm}^3$. It is a back-up to the CLBO crystal, in case the latter is damaged due to mechanic stress or absorption of water. The values for the BBO crystal parameters are taken from Tab. 3. The resulting values of the Boyd Kleinman integral h as a function of the phase mismatch factor σ and the focusing parameter ξ are shown are Fig. A.1a. The corresponding Figures for LBO and CLBO in the main text are Fig. 5.1a and Fig. 5.2a respectively. For BBO, the values for a maximum h are:

$$\begin{aligned} h_{\mathrm{BBO}} &= 0.0396 \\ \xi_{\mathrm{BBO}} &= 1.42 \\ \sigma_{\mathrm{BBO}} &= -0.75. \end{aligned} \tag{A.1}$$

We plot h as a function of ξ for $\sigma = 0$ and the optimum σ in Fig. A.1b. The maximum value for h in both cases only differs by a few percent. We therefore set σ to zero for simplicity. Also as explained in Sec. 5.1, we decrease ξ by a factor of 3 to avoid the damage threshold of the crystal and thermal lensing, changing the corresponding waist in the BBO crystal from $w = 19.6\,\mu\mathrm{m}$ to $w = 34.0\,\mu\mathrm{m}$. The final values used for later calculations are:

$$\begin{aligned} h_{\mathrm{BBO}} &= 0.0313 \\ \xi_{\mathrm{BBO}} &= 0.475 \\ \sigma_{\mathrm{BBO}} &= 0. \end{aligned} \tag{A.2}$$

We have optimized for a maximum single-pass conversion efficiency for a cavity with BBO and found the corresponding waist through the focusing parameter ξ.

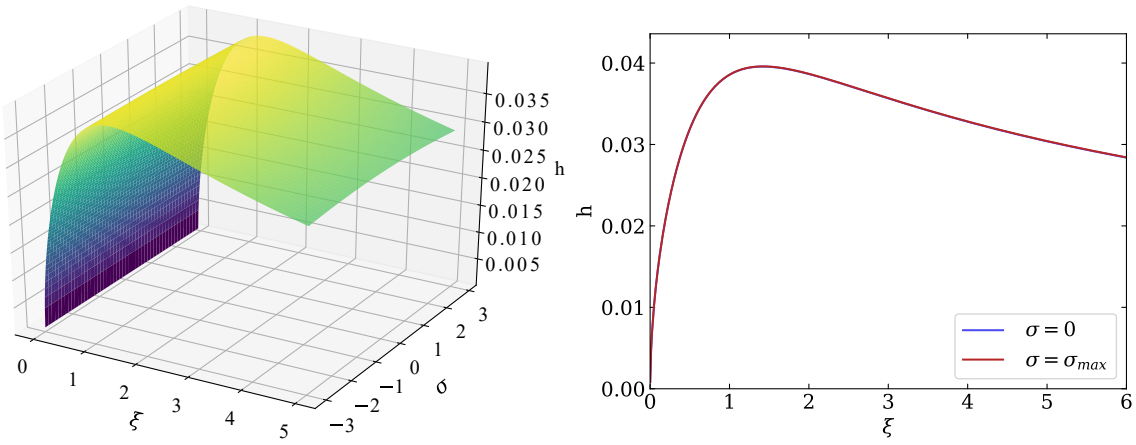

(a) Factor h as a function of ξ for $\sigma = 0$ and $\sigma_{max} = -0.75$

(b) Factor h as a function of ξ for $\sigma = 0$ and $\sigma_{max} = -0.75$: both curves lie almost exactly over each other

Figure A.1: Boyd-Kleinman factor h for the BBO crystal with material parameters from Tab. 3

The geometry optimization from Sec. 5.2 omits the calculations for a cavity with a Brewster-cut LBO crystal. The Brewster-cut LBO crystal is meant to be used in case the AR-coating of the other

LBO crystal is damaged due to high circulating power. The results of the geometry optimization for a cavity with a Brewster-cut LBO crystal are shown in the following. We optimize the geometry analogously to the calculations in Sec. 5.2. We start by choosing a mirror curvature of:

$$R_{,\,\mathrm{LBO,\,Brewster}} = 50\,\mathrm{mm}. \tag{A.3}$$

The ensuing values for the long and short arm are:

$$\begin{aligned} d_{s,\,\mathrm{LBO,\,Brewster}} &= 46.8\,\mathrm{mm} \\ d_{l,\,\mathrm{LBO,\,Brewster}} &= 185.3\,\mathrm{mm}. \end{aligned} \tag{A.4}$$

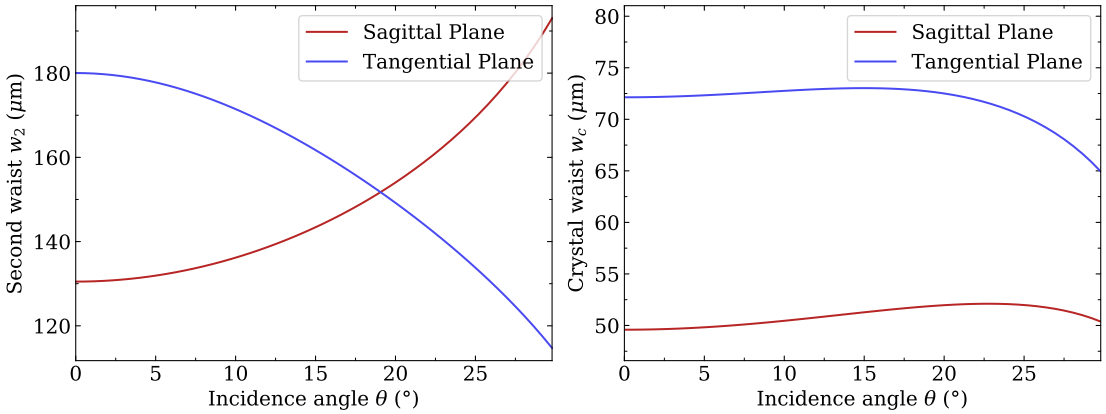

(a) Second waist in the long arm as a function of the incidence angle in the sagittal and tangential plane

(b) Crystal waist as a function of the incidence angle in the sagittal and tangential plane

Figure A.2: Waist sizes as a function of the opening angle θ for the geometric considerations with the Brewster-cut LBO crystal

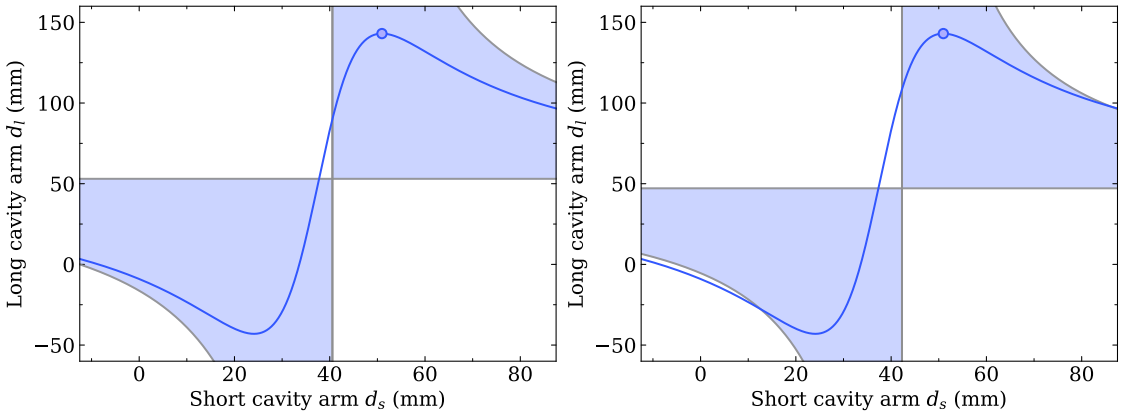

(a) Stability diagram in the sagittal plane as a function of the short and long arm d_s, d_l

(b) Stability diagram in the tangential plane as a function of the short and long arm d_s, d_l

Figure A.3: Differing stability diagrams in the tangential and sagittal plane for the Brewster-cut LBO crystal: the blue regions indicate a stable resonator, the blue curve is a result of the self-consistency condition and the point indicates the choice of arm lengths in this thesis

As for the AR-coated LBO crystal in Fig. 5.3 and the CLBO crystal in Fig. 5.4, we calculate the crystal and second waist in the sagittal and tangential plane and show the results in Fig. A.2. To

achieve a round second waist we choose:

$$\theta_{\text{LBO, Brewster}} = 20.8°. \tag{A.5}$$

As in Fig. 5.5 for the AR-coated LBO crystal and in Fig. 5.6 for the CLBO crystal, we plot the stability diagram for the Brewster-cut LBO crystal in the sagittal and tangential plane in Fig. A.3a and Fig. A.3b respectively. We confirm that the values for the long and short arm from Eq. A.4 lie within the stability region for the sagittal and tangential plane.

Finally, we show the results for impedance matching for the cavities with the AR coated LBO crystal and the BBO crystal omitted from Sec. 5.3. We calculate the efficiency as a function of the input reflectivity $\mathcal{R}_1$ for both crystals and show the results in Fig. A.4 for the Brewster-cut LBO crystal and in Fig. A.5 for the BBO crystal. We use the same input powers for the Brewster-cut LBO crystal as for the AR-coated alternative (see Fig. 5.7). For the calculation for BBO, the input powers are the same as the ones for CLBO (see Fig. 5.8). We use the same mirrors in the two doubling cavities, independent of the choice of crystals. Therefore we the values for the input reflectivity are the same as in Eq. 5.10:

$$\mathcal{R}_{1,\,\text{LBO, Brewster}} = 0.96 \pm 0.0075 \qquad \mathcal{R}_{1,\,\text{BBO}} = 0.985 \pm 0.005. \tag{A.6}$$

The uncertainty for $\mathcal{R}_1$ is shown as a grey area in the Figure and is a consequence of the manufacturing process of the mirrors.

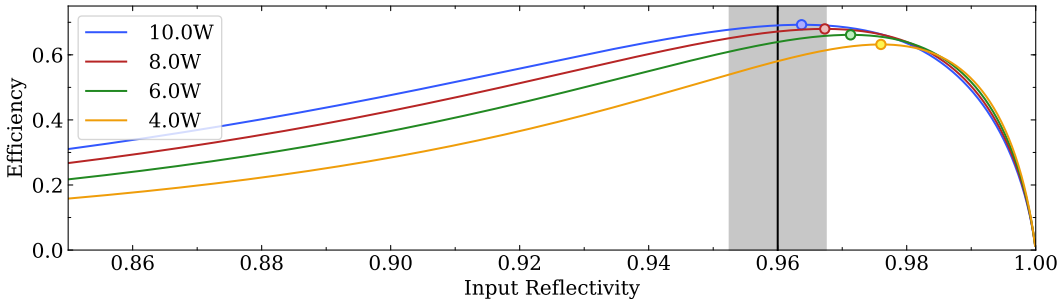

Figure A.4: Efficiency for varying values of the reflectivity $\mathcal{R}_1$ of the first mirror for the Brewster-cut LBO crystal, realistic input powers lie between 8 and 10 W

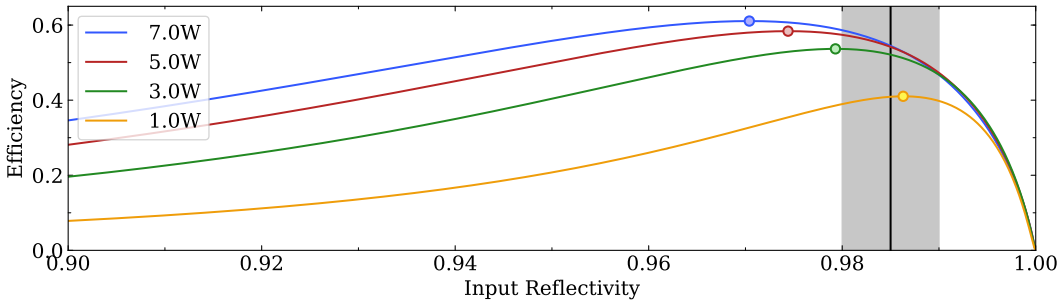

Figure A.5: Efficiency for varying values of the input reflectivity $\mathcal{R}_1$ of the first mirror for the BBO crystal, realistic input powers lie between 3 and 5 W

In this Appendix we have presented all calculations for the optimization of alternate cavities, omitted in Sec. 5.

Acknowledgements

First, I would like to thank Prof. Bloch for being my supervisor and for giving me the opportunity to join the MPQ, first as a working student and later as a master student.
I would also like to thank Prof. Gross for supervising my work and the great lectures that I still benefit from today.
Furthermore I would like to express my deepest gratitude to my direct supervisor Christian Gross for allowing me to work in his lab and always sharing his excitement over every progress, small and large alike. I would like to express my admiration at his capability to answer every question and find a solution to every problem.
I would also like to thank Nikolaus Lorenz for planning the project, always finding time to help and for not always giving the answer to keep me on my toes.
I would like to thank Lorenzo Festa for keeping me from breaking too many things in the lab.
I am also very lucky to have shared an office with Sarah Hirthe, who stayed sane even after being exposed to me for over a year.
I would like to thank Johannes Zeiher for his help with the calculation of the cavities and Jens Schultz Laustsen for his help optimizing the first one.
For his quick and reliable help on technical construction details, I am grateful to Anton Mayer.
I would like to thank the members of Bloch group for their hospitality and teaching me how to do midfield goals at the kicker table.
Last but not least, I would like to thank my parents and Clemens for bearing with me throughout this project and supporting me in each and every one of my decisions.

References

[1] M. H. Anderson, J. R. Ensher, M. R. Matthews, C. E. Wieman, and E. A. Cornell, "Observation of bose-einstein condensation in a dilute atomic vapor," *Science*, vol. 269, no. 5221, pp. 198–201, 1995.

[2] C. C. Bradley, C. Sackett, J. Tollett, and R. G. Hulet, "Evidence of bose-einstein condensation in an atomic gas with attractive interactions," *Phys. Rev. Lett.*, vol. 75, no. 9, p. 1687, 1995.

[3] K. B. Davis, M.-O. Mewes, M. R. Andrews, N. Van Druten, D. Durfee, D. Kurn, and W. Ketterle, "Bose-einstein condensation in a gas of sodium atoms," *Phys. Rev. Lett.*, vol. 75, no. 22, p. 3969, 1995.

[4] B. DeMarco and D. S. Jin, "Onset of fermi degeneracy in a trapped atomic gas," *Science*, vol. 285, no. 5434, pp. 1703–1706, 1999.

[5] F. Schreck, L. Khaykovich, K. Corwin, G. Ferrari, T. Bourdel, J. Cubizolles, and C. Salomon, "Quasipure bose-einstein condensate immersed in a fermi sea," *Phys. Rev. Lett.*, vol. 87, no. 8, p. 080403, 2001.

[6] A. G. Truscott, K. E. Strecker, W. I. McAlexander, G. B. Partridge, and R. G. Hulet, "Observation of fermi pressure in a gas of trapped atoms," *Science*, vol. 291, no. 5513, pp. 2570–2572, 2001.

[7] M. Greiner, O. Mandel, T. Esslinger, T. W. Hänsch, and I. Bloch, "Quantum phase transition from a superfluid to a mott insulator in a gas of ultracold atoms," *Nature*, vol. 415, no. 6867, p. 39, 2002.

[8] N. Navon, S. Nascimbene, F. Chevy, and C. Salomon, "The equation of state of a low-temperature fermi gas with tunable interactions," *Science*, vol. 328, no. 5979, pp. 729–732, 2010.

[9] J. Simon, W. S. Bakr, R. Ma, M. E. Tai, P. M. Preiss, and M. Greiner, "Quantum simulation of antiferromagnetic spin chains in an optical lattice," *Nature*, vol. 472, no. 7343, p. 307, 2011.

[10] W. S. Bakr, J. I. Gillen, A. Peng, S. Fölling, and M. Greiner, "A quantum gas microscope for detecting single atoms in a hubbard-regime optical lattice," *Nature*, vol. 462, no. 7269, p. 74, 2009.

[11] J. F. Sherson, C. Weitenberg, M. Endres, M. Cheneau, I. Bloch, and S. Kuhr, "Single-atom-resolved fluorescence imaging of an atomic mott insulator," *Nature*, vol. 467, no. 7311, p. 68, 2010.

[12] L. W. Cheuk, M. A. Nichols, M. Okan, T. Gersdorf, V. V. Ramasesh, W. S. Bakr, T. Lompe, and M. W. Zwierlein, "Quantum-gas microscope for fermionic atoms," *Phys. Rev. Lett.*, vol. 114, no. 19, p. 193001, 2015.

[13] E. Haller, J. Hudson, A. Kelly, D. A. Cotta, B. Peaudecerf, G. D. Bruce, and S. Kuhr, "Single-atom imaging of fermions in a quantum-gas microscope," *Nat. Phys.*, vol. 11, no. 9, p. 738, 2015.

[14] M. F. Parsons, F. Huber, A. Mazurenko, C. S. Chiu, W. Setiawan, K. Wooley-Brown, S. Blatt, and M. Greiner, "Site-resolved imaging of fermionic li 6 in an optical lattice," *Phys. Rev. Lett.*, vol. 114, no. 21, p. 213002, 2015.

[15] A. Omran, M. Boll, T. A. Hilker, K. Kleinlein, G. Salomon, I. Bloch, and C. Gross, "Microscopic observation of pauli blocking in degenerate fermionic lattice gases," *Phys. Rev. Lett.*,

vol. 115, no. 26, p. 263001, 2015.

[16] G. Edge, R. Anderson, D. Jervis, D. McKay, R. Day, S. Trotzky, and J. Thywissen, "Imaging and addressing of individual fermionic atoms in an optical lattice," *Phys. Rev. A*, vol. 92, no. 6, p. 063406, 2015.

[17] C. Weitenberg, M. Endres, J. F. Sherson, M. Cheneau, P. Schauß, T. Fukuhara, I. Bloch, and S. Kuhr, "Single-spin addressing in an atomic mott insulator," *Nature*, vol. 471, no. 7338, p. 319, 2011.

[18] T. Fukuhara, A. Kantian, M. Endres, M. Cheneau, P. Schauß, S. Hild, D. Bellem, U. Schollwöck, T. Giamarchi, C. Gross, *et al.*, "Quantum dynamics of a mobile spin impurity," *Nat. Phys.*, vol. 9, no. 4, p. 235, 2013.

[19] P. Zupancic, P. M. Preiss, R. Ma, A. Lukin, M. E. Tai, M. Rispoli, R. Islam, and M. Greiner, "Ultra-precise holographic beam shaping for microscopic quantum control," *Opt. Express*, vol. 24, no. 13, pp. 13881–13893, 2016.

[20] S. Baier, M. J. Mark, D. Petter, K. Aikawa, L. Chomaz, Z. Cai, M. Baranov, P. Zoller, and F. Ferlaino, "Extended bose-hubbard models with ultracold magnetic atoms," *Science*, vol. 352, no. 6282, pp. 201–205, 2016.

[21] K. Aikawa, A. Frisch, M. Mark, S. Baier, A. Rietzler, R. Grimm, and F. Ferlaino, "Bose-einstein condensation of erbium," *Phys. Rev. Lett.*, vol. 108, no. 21, p. 210401, 2012.

[22] M. Lu, N. Q. Burdick, S. H. Youn, and B. L. Lev, "Strongly dipolar bose-einstein condensate of dysprosium," *Phys. Rev. Lett.*, vol. 107, no. 19, p. 190401, 2011.

[23] A. Griesmaier, J. Werner, S. Hensler, J. Stuhler, and T. Pfau, "Bose-einstein condensation of chromium," *Phys. Rev. Lett.*, vol. 94, no. 16, p. 160401, 2005.

[24] K. R. Hazzard, B. Gadway, M. Foss-Feig, B. Yan, S. A. Moses, J. P. Covey, N. Y. Yao, M. D. Lukin, J. Ye, D. S. Jin, *et al.*, "Many-body dynamics of dipolar molecules in an optical lattice," *Phys. Rev. Lett.*, vol. 113, no. 19, p. 195302, 2014.

[25] R. Löw, H. Weimer, J. Nipper, J. B. Balewski, B. Butscher, H. P. Büchler, and T. Pfau, "An experimental and theoretical guide to strongly interacting rydberg gases," *J. Phys. B*, vol. 45, no. 11, p. 113001, 2012.

[26] S. Hirthe, "A laser setup for two-photon rydberg excitation of potassium," Master's thesis, Ludwig-Maximilians-Universität München, 2018.

[27] T. F. Gallagher, *Rydberg atoms*, vol. 3. Cambridge University Press, 2005.

[28] M. Seaton, "Quantum defect theory," *Rep. Prog. Phys*, vol. 46, no. 2, p. 167, 1983.

[29] W. Li, I. Mourachko, M. Noel, and T. Gallagher, "Millimeter-wave spectroscopy of cold rb rydberg atoms in a magneto-optical trap: Quantum defects of the ns, np, and nd series," *Phys. Rev. A*, vol. 67, no. 5, p. 052502, 2003.

[30] N. Šibalić, J. D. Pritchard, C. S. Adams, and K. J. Weatherill, "Arc: An open-source library for calculating properties of alkali rydberg atoms," *Comput. Phys. Comm.*, vol. 220, pp. 319–331, 2017.

[31] T. G. Tieck, *Feshbach resonances in ultracold mixtures of the fermionic quantum gases 6Li and 40K*. PhD thesis, Univeristy of Amsterdam, 2009.

[32] C. Chin, R. Grimm, P. Julienne, and E. Tiesinga, "Feshbach resonances in ultracold gases," *Reviews of Modern Physics*, vol. 82, no. 2, p. 1225, 2010.

[33] H. Ritsch, P. Domokos, F. Brennecke, and T. Esslinger, "Cold atoms in cavity-generated dynamical optical potentials," *Rev. Mod. Phys.*, vol. 85, no. 2, p. 553, 2013.

[34] J. Zeiher, *Realization of Rydberg-dressed quantum magnets*. PhD thesis, Ludwig-Maximilians-Universität München, 2017.

[35] J. Johnson and S. Rolston, "Interactions between rydberg-dressed atoms," *Phys. Rev. A*, vol. 82, no. 3, p. 033412, 2010.

[36] T. H. Maiman *et al.*, "Stimulated optical radiation in ruby," 1960.

[37] P. Franken, A. E. Hill, C. e. Peters, and G. Weinreich, "Generation of optical harmonics," *Phys. Rev. Lett.*, vol. 7, no. 4, p. 118, 1961.

[38] R. W. Boyd, *Nonlinear optics*. Elsevier, 2003.

[39] G. Rempe, "Quantum optics," 2017.

[40] P. Milonni and J. H. Eberly, "Laser physics," 2010.

[41] G. Boyd and D. Kleinman, "Parametric interaction of focused gaussian light beams," *J. Appl. Phys.*, vol. 39, no. 8, pp. 3597–3639, 1968.

[42] W. P. Risk, W. P. Risk, T. Gosnell, and A. Nurmikko, *Compact blue-green lasers*. Cambridge University Press, 2003.

[43] A. E. Siegman, "Lasers university science books," *Mill Valley, CA*, vol. 37, p. 208, 1986.

[44] H. Kogelnik and T. Li, "Laser beams and resonators," *App. Opt.*, vol. 5, no. 10, pp. 1550–1567, 1966.

[45] A. Yariv, "Quantum electronics," *3rd Edn. (John Wiley & Sons, New York, 1988) p*, vol. 389, 1989.

[46] D. Hanna, "Astigmatic gaussian beams produced by axially asymmetric laser cavities," *IEEE J. Quantum Eletron.*, vol. 5, no. 10, pp. 483–488, 1969.

[47] B. E. Saleh, M. C. Teich, and B. E. Saleh, *Fundamentals of photonics*, vol. 22. Wiley New York, 1991.

[48] E. D. Black, "An introduction to pound–drever–hall laser frequency stabilization," *Am. J. Phys.*, vol. 69, no. 1, pp. 79–87, 2001.

[49] T. Hansch and B. Couillaud, "Laser frequency stabilization by polarization spectroscopy of a reflecting reference cavity," *Opt. Comm.*, vol. 35, no. 3, pp. 441–444, 1980.

[50] H.-M. Meyer, "A laser-system for trapping and cooling of ytterbium-ions," Master's thesis, University of Heidelberg, 2010.

[51] Y. Yap, T. Inoue, H. Sakai, Y. Kagebayashi, Y. Mori, T. Sasaki, K. Deki, and M. Horiguchi, "Long-term operation of cslib 6 o 10 at elevated crystal temperature," *Opt. Lett.*, vol. 23, no. 1, pp. 34–36, 1998.

[52] A. Smith, "Snlo software package," *www. as-photonics. com*, 2008.

[53] T. Beck, B. Rein, F. Sörensen, and T. Walther, "Solid-state-based laser system as a replacement for ar+ lasers," *Opt. Lett.*, vol. 41, no. 18, pp. 4186–4189, 2016.

[54] Z. Burkley, C. Rasor, S. Cooper, A. Brandt, and D. Yost, "Yb fiber amplifier at 972.5 nm with frequency quadrupling to 243.1 nm," *Appl. Phys. B*, vol. 123, no. 1, p. 5, 2017.

[55] Y. Kaneda, J. Yarborough, L. Li, N. Peyghambarian, L. Fan, C. Hessenius, M. Fallahi, J. Hader,

J. V. Moloney, Y. Honda, *et al.*, "Continuous-wave all-solid-state 244 nm deep-ultraviolet laser source by fourth-harmonic generation of an optically pumped semiconductor laser using cslib 6 o 10 in an external resonator," *Opt. Lett.*, vol. 33, no. 15, pp. 1705–1707, 2008.

[56] J. Sakuma, Y. Asakawa, and M. Obara, "Generation of 5-w deep-uv continuous-wave radiation at 266 nm by an external cavity with a cslib 6 o 10 crystal," *Opt. Lett.*, vol. 29, no. 1, pp. 92–94, 2004.

[57] T. Südmeyer, Y. Imai, H. Masuda, N. Eguchi, M. Saito, and S. Kubota, "Efficient 2 nd and 4 th harmonic generation of a single-frequency, continuous-wave fiber amplifier," *Opt. Express*, vol. 16, no. 3, pp. 1546–1551, 2008.

[58] J. Alnis, A. Matveev, N. Kolachevsky, T. Udem, and T. Hänsch, "Subhertz linewidth diode lasers by stabilization to vibrationally and thermally compensated ultralow-expansion glass fabry-pérot cavities," *Phys. Rev. A*, vol. 77, no. 5, p. 053809, 2008.

[59] T. C. Briles, D. C. Yost, A. Cingöz, J. Ye, and T. R. Schibli, "Simple piezoelectric-actuated mirror with 180 khz servo bandwidth," *Opt. Express*, vol. 18, no. 10, pp. 9739–9746, 2010.